

Re-observing the NLS1 Galaxy RE J1034+396. II. New Insights on the Soft X-ray Excess, QPO and the Analogy with GRS 1915+105

Chichuan Jin^{1,2,*}, Chris Done³, Martin Ward³

¹National Astronomical Observatories, Chinese Academy of Sciences, 20A Datun Road, Beijing 100101, China

²School of Astronomy and Space Sciences, University of Chinese Academy of Sciences, 19A Yuquan Road, Beijing 100049, China

³Centre for Extragalactic Astronomy, Department of Physics, University of Durham, South Road, Durham DH1 3LE, UK

prepared for MNRAS

ABSTRACT

RE J1034+396 displays the so far detected most significant X-ray Quasi-Periodic Oscillation (QPO) in AGN. We perform a detailed spectral-timing analysis on the data using recent simultaneous *XMM-Newton*, *NuSTAR* and *Swift* observations. We present the detailed energy dependence of the QPO's frequency, rms, coherence and phase lag. We construct various frequency-resolved variability spectra, which are modelled together with the time-averaged spectra. Our study shows that four components are required to fit all the spectra, including an inner disc component (`diskbb`), two warm corona components (`CompTT-1` and `CompTT-2`) and a hot corona component (`nthComp`). An important discovery is that within the two warm corona components, `CompTT-2` (the hotter, less luminous component) contains the QPO signal, while the stochastic variability is concentrated in `CompTT-1`. These components also allow us to fit the lag-energy spectra, as well as being able to describe the previous observation of a strong QPO in 2007, and the absent QPO observations, by varying only the relative normalizations of these components. Our multi-wavelength study shows that the QPO's detectability does not depend on the contemporaneous mass accretion rate through the outer disc as estimated from the UV flux. We do not detect a significant Iron $K\alpha$ line, nor any significant reflection component hump. Finally, we show that the rms and lag spectra of RE J1034+396 in the recent observation are very similar to the 67 Hz QPO in the micro-quasar GRS 1915+105. These new results reinforce the physical analogy between the two sources. We speculate that the QPO in both sources is due to expansion/contraction of the inner disc vertical structure.

Key words: accretion, accretion discs - galaxies: active - galaxies: nuclei.

1 INTRODUCTION

The Quasi-Periodic Oscillation (QPO) in the Narrow Line Seyfert 1 galaxy RE J1034+396 ($z = 0.0424$) is the most significant and persistent example of an X-ray QPO in any Active Galactic Nuclei (AGN: see Figure 1). It has been seen in multiple observations spanning more than 10 years (Gierliński et al. 2008, Middleton et al. 2009, Alston et al. 2014, Jin, Done & Ward 2020, hereafter referred to as Paper-I). Clearly, a key question is what is so special about RE J1034+396 that results in such a dramatic QPO? One possible answer is that it is in some way related to the extraordinarily strong soft X-ray excess present in this AGN (Puch-

narawicz et al. 1995). The soft excess is defined as the additional emission over and above an extrapolation of the best-fit hard X-ray power law to the spectrum below 2 keV, and is ubiquitously seen in AGN which lack a significant gas column density (e.g. Arnaud et al. 1985; Turner & Pounds 1988, Porquet et al. 2004, Gierliński & Done 2004, Crummy et al. 2006). However, the origin of this component remains a classic unsolved problem, especially as it has no obvious analog in X-ray binaries (e.g. Kubota, Makishima & Ebisawa 2001; Kubota & Done 2004; Page et al. 2004). Currently, there exists most favoured spectral models. The first one is that there is an additional warm, optically thick Comptonisation emission region as well as the hot, optically thin Comptonisation which produces the hard X-ray emission (e.g. Porquet et al. 2004, Gierliński & Done 2004, Petrucci et al. 2018),

*E-mail: ccjin@nao.cas.cn

probably part of the disc itself where the emission does not completely thermalise (Kubota & Done 2018). The alternative one is that it arises from harder X-ray illumination of the partially ionised accretion disc. This would imply that the soft X-ray reflected/reprocessed spectrum should be dominated by atomic features, but their presence smeared out by strong relativistic effects (Ross & Fabian 1993; Ballantyne, Ross & Fabian 2001; Crummy et al. 2006; Kara et al. 2016). Despite these models being physically very different, they still cannot be easily distinguished by spectral fitting alone, especially over the limited 0.3-10 keV bandpass of the X-ray data.

The soft X-ray excess is strongest in the subset of AGN classified as Narrow Line Seyfert 1 galaxy (NLS1, e.g. Boller, Brandt & Fink 1996). However, NLS1s often have low black hole masses and high mass accretion rates (e.g. Boroson 1992), so they are also the systems with the highest predicted intrinsic disc temperatures in AGN. In RE J1034+396 the inner disc is predicted to emit in the soft X-ray bandpass, so part of its very steep soft X-ray spectrum can arise from the disc itself (Jin et al. 2012a, Done et al. 2012). Hence, there can potentially exist four components in the X-ray spectrum of RE J1034+396, namely the intrinsic disc emission, the soft excess, and the hard X-ray power law and its reflection/reprocessed emission from the illuminated disc. In this paper we will explore how the QPO affects each of these components in an attempt to constrain its physical origin.

Since the spectral fitting procedure is degenerate, we must include some additional information contained in the variability characteristics to deconvolve these components. There are a variety of spectral-timing techniques available (Uttley et al. 2014). Some of these explore the level of variability for a given timescale as a function of energy (e.g. rms spectra and energy-resolved power spectra), while more powerful techniques search for correlated variability across different energy bands. Such correlations are valuable not only technically as it enhances the signal-to-noise (S/N), but also physically as it provides clues to the causality. For example, if the soft X-ray excess results solely from illumination of the disc by the variable hard X-ray corona, then the soft X-ray variability should be associated with that of the harder X-rays, but smoothed and lagged by the light travel timescale, e.g. a reverberated soft X-ray lag (Fabian et al. 2009). Conversely, if it is a separate additional component, it will most likely vary independently of the hard X-rays. However, if this is due to mass accretion rate fluctuations then this should propagate inwards on the viscous timescale, and then modulate the mass accretion rate in the hard X-ray emission region, e.g. propagation with a soft X-ray lead (Kotov, Churazov & Gilfanov 2010; Arévalo & Uttley 2006).

Previous applications of these correlation techniques applied to NLS1s have shown that both of the above two effects are important. The correlated variability shows a soft lead for long timescale fluctuations, and a soft lag at the shortest timescales (Fabian et al. 2009; Emmanoulopoulos, McHardy & Papadakis 2011; Zoghbi et al. 2013; Kara et al. 2017; Parker, Miller & Fabian 2018). This probably implies that the soft X-ray excess contains both slow variability of intrinsic soft X-ray emission which propagates inwards, and fast variability of the intrinsic hard X-ray component which reverberates. For example, a complete spectral-timing model of this physical picture can fit the full range of spec-

tral/timing properties of the simple NLS1 PG 1244+026 (Gardner & Done 2014, hereafter GD14), including the spectrum of the fastest variability (Jin et al. 2013).

In Paper-I we show that the QPO in a recent *XMM-Newton* observation of RE J1034+396 in 2018 (Obs-9) is strong and highly coherent. There is a clear soft X-ray variation lead at the QPO frequency, which is the opposite to the results from a previous observation in 2007 (Obs-2) as shown in Zoghbi & Fabian (2011). This soft X-ray lead in the QPO makes analogy between this QPO and the strong 67 Hz QPO seen the stellar mass black hole GRS 1915+105 more convincing (Middleton et al. 2009; Middleton, Uttley & Done 2011; Méndez et al. 2013).

Here we use a range of spectral-timing techniques (both time-averaged and correlated) to explore both the standard AGN stochastic variability and the QPO component present in the *XMM-Newton* data, and show how these can be used to help break the degeneracies in spectral modelling of the soft X-ray excess. In addition we have *NuSTAR* data which extends the available spectral bandpass with relatively good S/N up to ~ 40 keV, which strongly constrains any reflection component present in the data (Sections 3 and 4). The best-fit model is then applied to previous observations as a further test and consistency check (Section 5). We also explore the broadband spectral energy distribution of RE J1034+396, as well as its long term UV variability measured simultaneously with the X-ray data by the *XMM-Newton* OM (Section 6). We make a detailed comparison with the 67 Hz QPO from GRS 1915+105 in Section 7, and discuss physical models for the origin of the QPO in Section 8. The final section summarizes the main results of this paper.

Throughout this work we adopt a flat universe model with the Hubble constant $H_0 = 72 \text{ km s}^{-1} \text{ Mpc}^{-1}$, $\Omega_\Lambda = 0.73$ and $\Omega_M = 0.27$. All the spectral fittings are performed with the XSPEC software (v12.11.01, Arnaud 1996).

2 OBSERVATIONS AND DATA REDUCTION

2.1 *XMM-Newton*

XMM-Newton (Jansen et al. 2001) has observed RE J1034+396 9 times (Paper-I). In this paper, we make use of data from Obs-2, 3, 6 and 9. Obs-2 and 9 provide data of much higher quality than the other observations in terms of both long exposure times and low background, and so the QPO in these two observations can be studied in considerable detail. Obs-3 and 6 are the two observations catching RE J1034+396 in its non-QPO state. As described in Paper-I, we downloaded the data from the *XMM-Newton* Science Archive (XSA), and re-reduced the data using the *XMM-Newton* Science Analysis System (SAS v18.0.0) with the most recent calibration files. The procedures used for all the observations are the same. We define a circular source extraction region of 80 arcsec radius. Obs-2 suffers from significant pile-up and so we exclude a circular region of 10 arcsec radius around the source position when pile-up should be considered (see Appendix B). The EPPROC, EMPROC and EVSELECT scripts were used to reduce the data from European Photon Imaging Camera (EPIC) and extract spectra and light curves. The RGSPROC script was used to reprocess the data from the Reflection Grating Spectrometer (RGS)

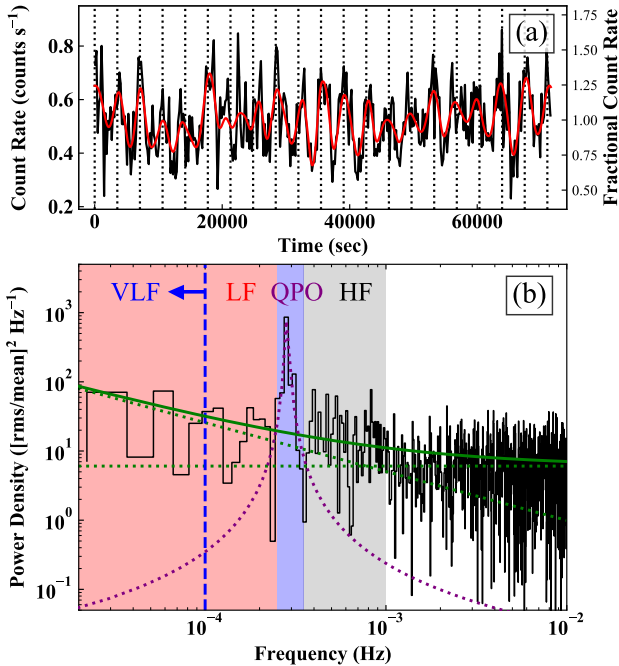


Figure 1. Panel-a: the 1-4 keV light curve of RE J1034+396 in the *XMM-Newton* EPIC-pn observation in 2018 (Obs-9). The red solid line shows the QPO component as represented by the intrinsic mode function (see Paper-I). Vertical dotted lines show a period of 3550 s. Panel-b: the PSD of the 1-4 keV light curve. The green solid line indicates the best-fit PSD continuum, which consists of a red-noise continuum and Poisson noise (green dotted lines). The purple dotted line indicates the best-fit lorentzian profile of the QPO. See Paper-I for further details. Four frequency bands have been defined, including the high-frequency band (HF): $(0.35 - 1.0) \times 10^{-3}$ Hz, QPO band: $(2.5 - 3.5) \times 10^{-4}$ Hz, low-frequency band (LF): $(0.14 - 2.5) \times 10^{-4}$ Hz, and very-low-frequency (VLF) band: $(0.14 - 1.0) \times 10^{-4}$ Hz. The lowest frequency is determined by the duration of the light curve.

and to extract the RGS spectra. The OMFCHAIN script was used to reprocess the data from the Optical Monitor (OM) and to extract the photometric flux through each filter that was used.

2.2 *NuSTAR*

NuSTAR (Harrison et al. 2013) performed an observation of RE J1034+396 in 2018-10-30 (Coordinated Universal Time: 10:29:38) for 100 ks exposure time, which overlapped with the entire observing window of the Obs-9 of *XMM-Newton*. We used the NUPIPELINE script in HEASOFT (v6.26.1, Blackburn 1995) to reprocess the data together with the most recent calibration database. To identify the South Atlantic Anomaly (SAA) passages and then remove contaminated data, we chose the `optimized` mode of SAA calculation with the default algorithm option 3. Then the NUSCREEN script was used to produce the cleaned event files with the GRADE range of 0-4. The source extraction region was chosen to be a circle with a radius of 1 arcmin centered on RE J1034+396. The background was extracted from an aperture of the same radius located on a nearby source-free region. The NUPRODUCTS script was used to ex-

tract the source and background spectra, and to produce the response and auxiliary files.

2.3 *Swift*

Swift performed a target-of-opportunity (ToO) observation of RE J1034+396 in 2018-10-30 for 1.7 ks exposure time, which was simultaneous with our *XMM-Newton* and *NuSTAR* campaign. We downloaded the data from the High Energy Astrophysics Science Archive (HEASARC), and reprocessed the data with HEASOFT (v6.26.1) and the most recent calibration files. We ran the XRPIPELINE to reprocess the X-ray Telescope (XRT) data and used the XSELECT tool to extract the spectrum from a circular region of 30 arcsec radius.

Six optical/UV filters were used by the ultraviolet-optical telescope (UVOT) during this observation, including UVW2, UVM2, UVW1, U, B, V. The host galaxy of RE J1034+396 is apparent in both the optical and UV bands, so we used a circular aperture of 10 arcsec radius to include both the AGN and host galaxy emission. The background flux was determined from a nearby source-free region with a circular radius of 40 arcsec. The UVOTSUM and UVOT-SOURCE scripts were run to extract the integrated sky image and source flux in each UVOT filter that was used in the observation. We also checked that our data are not affected by the small scale changes in sensitivity within the detector (Edelson et al. 2015)¹.

3 X-RAY SPECTRAL-TIMING PROPERTIES

3.1 Energy Dependence of the QPO Properties

In Paper-I we compared the QPO period and rms variability among 0.3-1, 1-4 and 2-10 keV bands, and found no significant change in the QPO period, but the fractional rms amplitude increased from 4% in 0.3-1 keV to 12.4% in 1-4 keV. In this paper, we divide the 0.3-10 keV band into smaller energy bins, and carry out a more comprehensive study into the energy dependences of the QPO's peak frequency, rms, time lag and coherence.

In order to determine the peak frequency of the QPO feature and its fractional rms amplitude, it is necessary to perform a careful modelling of the PSD. Following the same procedures in Paper-I, we use a power law to fit the red noise continuum, and a free constant to account for the Poisson noise. The QPO feature is modelled with a Gaussian profile. The maximum likelihood estimate (MLE) method is used to derive the best-fit parameters of the PSD model, and the rms is derived by integrating the best-fit QPO profile under the Belloni-Hasinger normalization (Belloni & Hasinger 1990). Based on the best-fit PSD model, we simulate 10^5 periodograms, and perform the same PSD fitting to each of them. Then the probability distributions of each model parameters are derived, from which their uncertainties are quantified.

Figure 2a shows the QPO frequency plotted against energy. We confirm our result in Paper-I but with a higher

¹ https://heasarc.gsfc.nasa.gov/docs/heasarc/caldb/swift/docs/uvot/uvotcaldb_sss_01.pdf

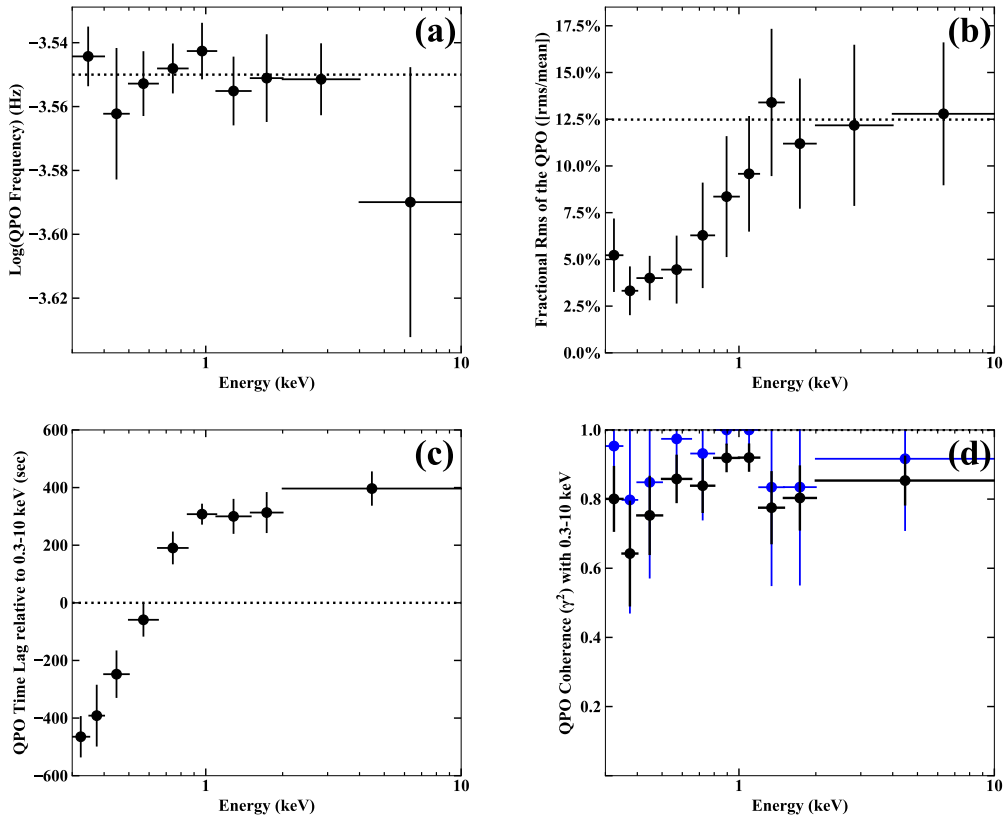


Figure 2. The energy dependences for selected QPO properties, including the QPO’s peak frequency (Panel-a), fractional rms amplitude (Panel-b), time lag relative to the QPO in 0.3-10 keV (Panel-c), and the coherence at the QPO frequency also relative to 0.3-10 keV (Panel-d). In Panel-a, the black dotted line indicate the QPO frequency of 2.8×10^{-4} Hz in 0.3-10 keV. In Panel-b, the black dotted line indicates the mean rms of 12.5 per cent above 2 keV. In Panel-c, positive values indicate lagging behind the reference band of 0.3-10 keV. In Panel-d, the black points are the raw coherences, while the blue points are the results after correcting for the Poisson noise. All the error bars represent 1σ uncertainties.

energy resolution, showing that the QPO’s peak frequency does not depend on the energy. Therefore, it is probable that the QPO signals present in different energy bands may have the same physical origin.

The fractional rms spectrum is shown in Figure 2b. This spectrum displays a typical shape for a NLS1. It rises from $\sim 3\%$ at 0.5 keV to 12% at 2 keV, and flattens towards the hard X-rays. Therefore, we can infer that the hard X-ray is dominated by a single component, and the soft excess contains a separate and less variable component. However, the ratio of rms between 2 keV and 0.3 keV is ~ 4 , while the ratio of flux in the time-averaged spectrum is ~ 16 , so there must be at least one component present in the soft X-ray excess which also contains the QPO.

In Paper-I we also reported the discovery that the QPO in 0.3-1 keV leads that in 1-4 keV by 430 s. We now investigate this in more detail by producing the lag spectrum. The QPO’s frequency bin is chosen to be $(2.5 - 3.5) \times 10^{-4}$ Hz, which includes 7 power spectral data points. The 0.3-0.4 keV band is selected to be the reference band. Figure 2c shows how the time lag changes with energy, where a positive lag indicates the 0.3-0.4 keV QPO leads. It is clear that the lag increases monotonically from 0.3 to 1 keV, and then flattens towards hard X-rays in a similar way to that of the rms spectrum. The maximum time lag between the soft and

hard bands is ~ 800 s. This shape of the QPO lag spectrum also supports the suggestion that the soft X-ray excess is dominated by a separate component from that of the hard X-rays.

Since a time lag between two time series is meaningful only if there is a strong coherence between them, we also calculate the coherence of the QPO relative to 0.3-0.4 keV and check its energy dependence. Figure 2d shows the raw coherence and the Poisson-noise-corrected coherence at different energies. It is clear that the QPO’s coherence is close to unity across 0.3-10 keV, which indicates that the QPO signals in different energy bands are highly coherent. Therefore, the phase lag of the QPOs should represent the true time lag between different energy bands. This further supports our claim in Paper-I that the positive QPO lag found in Obs-9 is more robust than the opposite time lag observed in Obs-2, because the QPO in Obs-2 has a much lower coherence.

3.2 Frequency-differentiated Non-QPO Variability Spectra

During Obs-9, RE J1034+396 shows strong stochastic variability as well as the presence of the QPO. Here we explore the spectral-timing properties of the stochastic variability,

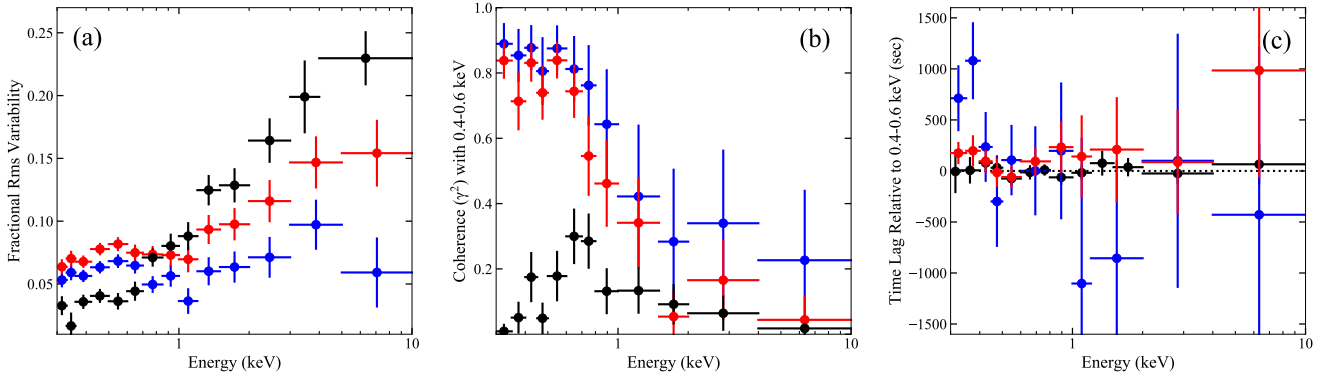


Figure 3. Panel-a: fractional rms spectra for the low-frequency band (red points), high-frequency band (black points) and very-low-frequency band (blue). Panel-b: coherence spectra relative to the 0.4-0.6 keV band for the same three frequency bands. Panel-c: lag spectra relative to the 0.4-0.6 keV band for the same three frequency bands. The definition of various frequency bands is given in Figure 1.

and compare them with those of the QPO. We define a low-frequency (LF) range as $(0.14 - 2.5) \times 10^{-4}$ Hz, where the lower frequency limit is determined by the duration of the clean light curve. The high-frequency (HF) range is set to be $(0.35 - 1.0) \times 10^{-3}$ Hz. These frequency ranges are set to completely exclude the QPO signal. We also explore the very low frequency band, defined as $(0.14 - 1.0) \times 10^{-4}$ Hz (see shaded regions in Figure 1).

We note that due to the relative low count rate above 2 keV, there can exist a significant number of zero-count bins in the hard X-ray light curves if the binning time is too small (e.g. 50 s). These zero-count bins can severely bias the calculation of variability if not considered properly. One potential effect is that the high-frequency power can deviate significantly from Poisson due to the existence of these zero-count bins. Therefore, we choose a large binning time of 500 s to ensure that there are no zero-count bins in the light curves. This requirement imposes an upper limit of 10^{-3} Hz to the high frequency band.

First, we produce the fractional rms spectra at LF and HF, which are shown in Figure 3a as red and black spectra. The HF rms spectrum appears similar to that of the QPO below 1 keV (both in shape and normalization) but above 1 keV it continues to rise to a maximum above 20% at 10 keV (although with relatively low S/N), whereas the QPO flattens at $\sim 12\%$ from 1 keV onwards. The HF rms spectrum is similar to those seen in some other super-Eddington NLS1s which also have a smooth and steep soft X-ray excess (e.g. Jin et al. 2009; Jin, Done & Ward 2013), although so far no similarly significant QPOs have been detected from these NLS1s, in the present case of RE J1034+396.

The LF stochastic variability rms spectrum is rather different from both the HF and the QPO. It has a hump below 1 keV, and then a gradual increase towards hard X-rays. Its rms is higher than the HF in the soft X-rays, but lower than the HF in the hard X-rays. This suggests that the soft X-rays tend to vary more at lower frequencies than the hard X-rays, so they may originate from a more extended region (e.g. Gardner & Done 2014, Jin et al. 2017b). The rms of the VLF variability (blue) continues with this trend, but with even less variability above 2 keV.

We select the high S/N 0.4-0.6 keV light curve as the reference band to produce the coherence and lag spectra (Pan-

els b and c in Figure 3) for HF (black), LF (red) and VLF (blue). There is almost no coherence at the HF (black), and in addition the HF lags are not statistically significant. In contrast, the slower stochastic variability at LF (red) varies coherently across the 0.3-0.7 keV energy range, and then drops rapidly to zero towards 1 keV and at higher energies. Therefore, the LF variability of the soft X-rays is not correlated with the hard X-rays, and there is no significant LF time lag across the 0.3-10 keV band, either. This is somewhat different situation from that observed in some other super-Eddington NLS1s, for example, PG 1244+026 and RX J0439.6-5311, in which it is found that the soft X-rays lead the hard X-rays at LF with a high coherence (Jin et al. 2013, 2017a). We point out that the X-ray flux of PG 1244+026 is higher than RE J1034+396 which, in turn, is higher than RX J0439.6-5311, and so this difference of LF time lag is not simply a result of the level of Poisson noise in the hard X-ray band.

Considering even slower variability (VLF: blue) there is potentially some correlated variability at 2-10 keV although none of the lags in this energy band are statistically significant. However, the VLF lags are marginally significant at lower energies, with the 0.3-0.35 keV band lagging behind 0.4-0.6 keV by 713 ± 313 s with a coherence of 0.89 ± 0.06 , while the 0.35-0.4 keV band lags by 1080 ± 367 s with a coherence of 0.85 ± 0.08 .

We also explored the situation using the 2-10 keV band as the reference light curve, as this band has high rms variability (see Figure 3a). The HF variability in 2-10 keV is also likely to be most sensitive to any soft X-ray reflection/reverberation processes arising from hard X-ray illumination of the inner disc, as well as the influence of the shape of the variable hard X-ray component (see e.g. Fig. 8 for the NLS1 PG 1244+026: Jin et al. 2013). However, unfortunately the S/N of the data is insufficient to determine the shape of the 2-10 keV emission component when this band is divided up into a higher energy resolution.

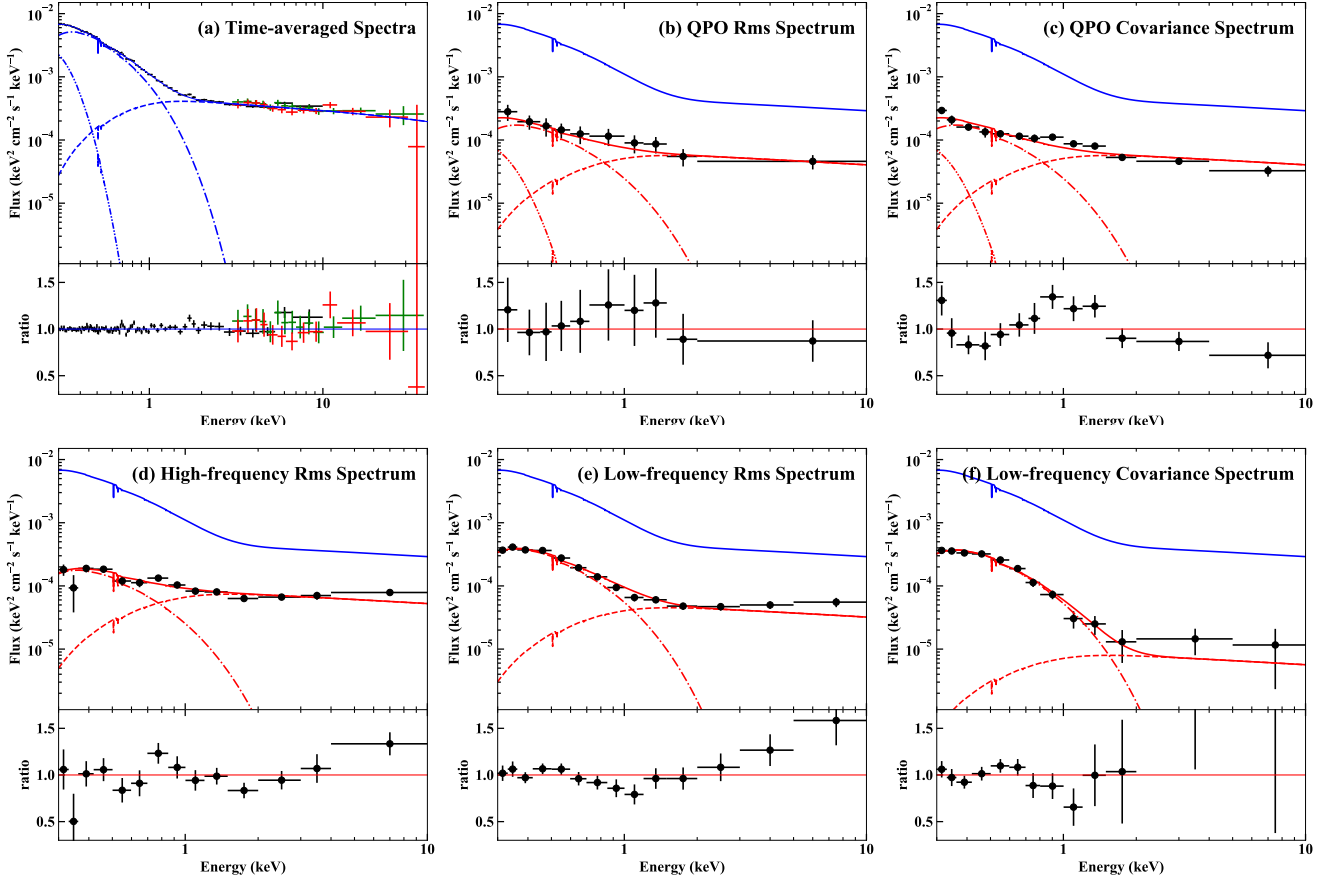


Figure 4. Simultaneous fits of the time-averaged spectra (Panel-a), rms spectrum (Panel-b) and covariance spectrum (Panel-c) at the QPO frequency, high-frequency rms spectrum (Panel-d), low-frequency rms spectrum (Panel-e), and low-frequency covariance spectrum (Panel-f) from Obs-9. The Model-1 configuration is used. In panel-a, the black, green and red spectra are from *XMM-Newton* EPIC-pn, *NuSTAR*/FPMA, *NuSTAR*/FPMB, respectively. The blue solid, dash, dash-dotted and dotted lines indicate the best-fit *nthComp*, *CompTT* and *diskbb* components, respectively. In Panels b-f, the red solid, dash, dash-dotted and dotted lines indicate their individual best-fit models and separate components, whose shapes are the same as in Panel-a, but with different normalizations. For comparison, the best-fit model of the time-averaged spectrum in Panel-a is also shown in the other panels as the blue solid line.

4 X-RAY SPECTRAL-TIMING MODELLING

4.1 Modelling the Time-averaged and Variability Spectra

Spectral fitting of the time-averaged spectrum of AGN is often degenerate, with very different physical models giving equally statistically good fits. Hence it is important to also include additional information from variability. The rms and coherence spectra reported here can be used together with the time-averaged spectra to provide the additional constraints from the spectral variability. For RE J1034+396 previous analysis on the time-averaged spectrum, QPO rms and covariance spectra from Obs-2 have shown that the soft X-rays are better explained by a warm, optically thick Comptonisation model than by relativistic reflection or absorption dominated models (Middleton et al. 2009; Middleton, Uttley & Done 2011). Such a warm corona model is also favoured for other NLS1s (e.g. Jin, Done & Ward 2013, 2016, 2017a; Kara et al. 2017; Parker, Miller & Fabian 2018).

There are 6 types of spectra which can be derived from the spectral-timing analysis described in the previous section. First, the time-averaged spectrum itself, then the ab-

solute rms spectrum, constructed by multiplying the fractional rms spectra by the time-average spectrum. We derive these for the QPO itself, and also for the HF and LF stochastic variability. The spectrum of the correlated variability is most clearly shown as covariance spectra, formed by multiplying the absolute rms spectra by the square root of the coherence (Uttley et al. 2014). Again we construct these for the QPO itself, and for the HF and LF stochastic variability, separately. But since there is no significant coherence for the HF stochastic variability, we do not show these data. In addition, we extend the time average-spectrum to higher energies using the *NuSTAR* spectrum observed simultaneously with *XMM-Newton* Obs-9.

4.1.1 Model-1: disc, soft X-ray & hard X-ray Comptonisation

The first model configuration (referred to as Model-1) includes an accretion disc component, a soft X-ray Comptonisation component and a hard X-ray Comptonisation component. These components are modeled by *diskbb*, *CompTT* (Titarchuk 1994) and *nthComp* (Zdziarski, Johnson &

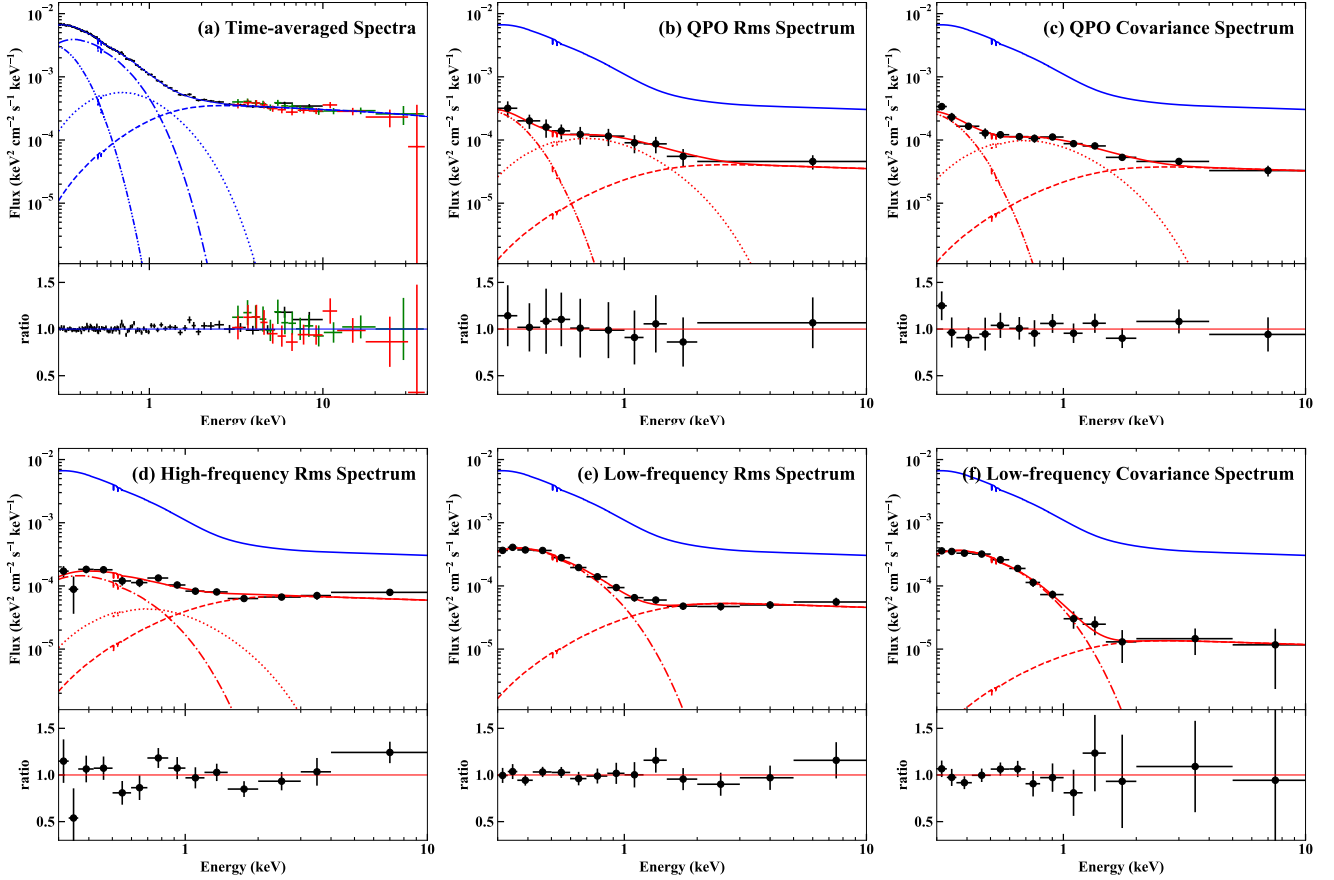


Figure 5. Similar to Figure 4, but for the Model-2 configuration, which produces good fits to all the spectra from Obs-9. The dash-dot-dot, dash-dot, dotted and dash lines indicate the `diskbb`, `ComPTT-1`, `ComPTT-2` and `nthComp` components, respectively.

Magdziarz 1996) in XSPEC, respectively. We further assume that the inner disk emission provides the seed photons for the soft X-ray Comptonisation which, in turn, provides seed photons for the hard X-ray Comptonisation. Thus the seed photon temperature of `ComPTT` is tied to the temperature of `diskbb`, and the seed photon temperature of `nthComp` is tied to the electron temperature of `ComPTT`. The electron temperature of `nthComp` is fixed at 200 keV. The Galactic X-ray absorption² ($N_{\text{H,gal}}$) towards RE J1034+396 is found to be $1.36 \times 10^{20} \text{ cm}^{-2}$ (Willingale et al. 2013), which is then modeled by the `TBabs` absorption model with the cross-sections taken from Verner et al. (1996) and abundances from Wilms, Allen & McCray (2000). The intrinsic neutral absorption of RE J1034+396 ($N_{\text{H,host}}$) is modelled by `zTBabs` as a free parameter. When fitting the variability spectrum we assume that they have the same model components as the time-averaged spectra, but with different normalizations. Furthermore, as a result of the QPO’s high coherence, the shapes of the two QPO spectra are consistent with each other, except that the covariance spectrum has smaller errors than the rms spectrum (Wilkinson & Uttley 2009). Thus we only adopt a free constant in order to account for their overall difference of normalizations.

We fit all these 6 types of spectra simultaneously assum-

ing that the model components differ only in their normalizations, but not in their shapes across all of the different types of spectra. We use this combined fit to obtain better constraints on the model parameters, with the best-fit results listed in Table 1, and the best-fit spectral decompositions shown in Figure 4.

We find that Model-1 fits the time-averaged spectra very well. The best-fit $N_{\text{H,host}}$ is found to be $2.95^{+1.49}_{-0.97} \times 10^{20} \text{ cm}^{-2}$, indicating a low amount of host galaxy absorption. The *NuSTAR* spectra show that the hard X-ray emission of RE J1034+396 has the form of a single power law up to 40 keV, with a photon index Γ of 2.20 ± 0.04 . There is no indication of either a reflection hump or high-energy cut-off. However the S/N is not sufficient to provide any useful spectral constraints above 40 keV. The best-fit disc emission has an inner temperature of $34.6^{+10.4}_{-4.9} \text{ eV}$. The electron temperature of `ComPTT` is found to be $0.20 \pm 0.02 \text{ keV}$, which is similar to the broadly constant value of $\sim 0.2 \text{ keV}$ found for many other AGN (Gierliński & Done 2004; Crummy et al. 2006; Jin et al. 2012a). The optical depth τ is found to be $12.4^{+2.1}_{-1.4}$, indicating an optically thick Comptonisation medium.

These components can also be used to fit the variability spectra, although there are some problems associated with these models, which are discussed in the next section. Figure 4 Panels-b and c show that the QPO rms and covariance spectra require contributions from all three compo-

² <https://www.swift.ac.uk/analysis/nhtot/index.php>

nents. The ratio of the overall normalization between these two variability spectra is 1.05 ± 0.17 , confirming that they are fully consistent with each other.

The HF and LF rms spectra only require contributions from **CompTT** and **nthComp**. The LF covariance spectrum is almost entirely dominated by the **CompTT** component, suggesting that although there is significant LF variability in the hard X-ray Comptonisation component, it is not significantly correlated with the LF variability in the soft X-ray Comptonisation component as would be expected if the soft X-ray Comptonisation variability propagates down into the hard X-ray Comptonisation region, either via viscous timescale mass accretion rate fluctuations, or as light travel time seed photon variability.

However, as suggested by the value of the the overall χ^2 of 704.4 for 653 dof, there is still some room to improve on the fits. Indeed, as shown in Figure 4 Panels-b and c, the QPO's variability spectra exhibit an extra hump at ~ 1 keV, implying that the best-fit **CompTT** may have a too low electron temperature or too small optical depth. This problem was also noted by Middleton, Uttley & Done (2011), who analyzed the QPO covariance spectrum from Obs-2. These authors suggested that the soft excess in the QPO covariance spectrum could indicate the presence of an additional soft X-ray Comptonisation component, with a temperature higher than that required in the time-averaged spectrum. Changes in the shape of the soft X-ray Comptonisation emission is also suggested by the LF rms spectrum, where the best-fit **CompTT** over-predicts the emission around 1 keV. There are also some difficulties with the hard X-ray Comptonisation component between these different types of spectra. These issues lead us to further explore the effect of an additional soft X-ray Comptonisation component.

4.1.2 Model-2: disc, soft X-ray & hard X-ray Comptonisation, plus an extra intermediate Comptonisation

In order to improve the fits shown in Figure 4, we propose that there exists an intermediate Comptonisation region between the soft and hard X-ray Comptonisation regions. In this new model there is now a **diskbb** component, which provides the seed photons for the first Comptonisation component (**CompTT-1**), which provides the seed photons for a second Comptonisation component (**CompTT-2**), which in turn provides the seed photons for the hard X-ray Comptonisation component (**nthComp**). All of the previous model configurations and assumptions remain the same. Similarly, we fit all of the 6 types of spectra simultaneously, only allowing the normalizations of the spectral components to vary when fitting the variability spectra. The best-fit parameters are listed in Table 1. In comparison with Model-1, the overall χ^2 of Model-2 decreases by 51.2 for 7 extra free parameters, indicating 5.8σ improvement of the fitting. Therefore, Model-2 provides a significant improvement to the fit, and more importantly it allows the fitting issues of Model-1 highlighted above to be addressed.

Fitting of the time-averaged spectra is similarly good as for Model-1, although the best-fit parameters are very different because of the inclusion of an additional component. In Model-2, the best-fit $N_{\text{H,host}}$ decreases to $1.20^{+3.83}_{-1.20} \times 10^{20}$

cm^{-2} , and the temperature of **diskbb** increases to $52.2^{+7.9}_{-19.1}$ eV. **CompTT-1** dominates the soft excess below 1 keV, with a lower electron temperature of $0.14^{+0.01}_{-0.02}$, and a larger optical depth of $20.2^{+4.0}_{-4.9}$. **CompTT-2** dominates the flux within 1-2 keV, with a higher electron temperature of $0.33^{+0.10}_{-0.11}$ and an optical depth of $12.5^{+11.7}_{-2.5}$. **nthComp** still dominates the hard X-rays above 2 keV, with a best-fit photon index of 2.11 ± 0.05 .

The main improvement of Model-2 lies in the fits to all the variability spectra, as shown in Figure 5. Especially, the QPO and stochastic LF variability split the spectral components in the soft excess. The soft X-ray Comptonisation in the QPO is consistent with only the hotter soft X-ray Comptonisation component (**CompTT-2**), whereas that in the LF variability is consistent with only the cooler soft X-ray Comptonisation component (**CompTT-1**). Only the HF rms spectrum (and time-averaged spectra) require both **CompTT-1** and **CompTT-2**. The QPO spectrum also includes a contribution from the disc, which is not seen in either HF or LF stochastic variability spectra. All spectra also exhibit some contribution from **nthComp**, but this has a higher seed photon temperature than in Model-1, which is now set by the electron temperature of **CompTT-2**. Table 2 lists the fractional normalizations of spectral components in each variability spectrum for the best-fit Model-2.

We can allow a greater range of freedom for the seed photon temperature between the various components as it is possible that both **diskbb** and **CompTT-1** can provide seed photons for **CompTT-2**, and that **diskbb**, **CompTT-1** and **CompTT-2** can provide seed photons for **nthComp**. Therefore, we set the seed photon temperature of **CompTT-2** and **nthComp** as free parameters (hereafter: Model-2b), and then check if the fitting can be improved. Table 1 shows the new fitting results. In this case, the new χ^2 decreases by 5.4 for 2 dof, equivalent to a 1.8σ significance. Thus the fitting is not improved significantly. The seed photon temperature of **CompTT-2** is found to be $0.14^{+0.03}_{-0.04}$ KeV, which is still consistent with the electron temperature of **CompTT-1**. But now the electron temperature of **CompTT-2** increases significantly to 1.98 keV (although poorly constrained), which is much larger than the best-fit seed photon temperature of **nthComp**. So it is indeed possible that **nthComp** can receive seed photons from each of the soft X-ray components. The temperature of **diskbb** decreases to $30.5^{+8.1}_{-3.9}$ eV, so its contribution in the soft excess is smaller. Despite these differences in the best-fit parameters, the spectral decompositions of Model-2b are generally similar to those for Model-2, so we do not plot the fitting results separately.

4.2 Modelling the QPO's Lag Spectrum

We can explore further the appropriateness of our best-fit spectral decompositions above by fitting them to the QPO lag spectrum (Figure 2c). We assume that the shape of the lag spectrum is produced by the relative contributions of the various spectral components in different energy bins, and fit for the lags between these various components required to fit the normalization and shape of the lag spectrum.

First we test the spectral decomposition of the best-fit Model-1. As shown in Figure 4a, the **diskbb** component has a very small flux contribution in the time-averaged spec-

Table 1. The best-fit parameters of Model-1, Model-2 and Model-2b. $N_{\text{H,gal}}$ and $N_{\text{H,ins}}$ are the Galactic absorption column and intrinsic absorption column of RE J1034+396, separately. ‘f’ indicates that this parameter is fixed. For linked parameters, we put the parameter names in the table instead of values. The error bars indicate 90 percent confidence limits.

Comp.	Par.	Model-1	Model-2	Model-2	Model-2b	Model-2b	Unit
		Obs-9	Obs-9	Obs-2	Obs-9	Obs-2	
TBabs	$N_{\text{H,gal}}$	1.36 (f)	10^{20} cm^{-2}				
zTBabs	$N_{\text{H,host}}$	$2.95^{+1.49}_{-0.97}$	$1.20^{+3.83}_{-1.20}$	$2.59^{+0.63}_{-0.65}$	$5.34^{+2.27}_{-2.08}$	$5.88^{+1.07}_{-1.08}$	10^{20} cm^{-2}
diskbb	T_{in}	$34.6^{+10.4}_{-4.9}$	$52.2^{+7.9}_{-19.1}$	52.2 (f)	$30.5^{+8.1}_{-3.9}$	30.5 (f)	eV
diskbb	$norm$	$1.24^{+9.76}_{-1.19} \times 10^7$	$3.60^{+533.37}_{-2.57} \times 10^5$	$4.31^{+1.00}_{-0.94} \times 10^5$	$0.13^{+1.23}_{-0.12} \times 10^9$	$1.06^{+0.58}_{-0.46} \times 10^8$	
compTT-1	T_0	diskbb- T_{in}	eV				
compTT-1	kT	$0.20^{+0.02}_{-0.02}$	$0.14^{+0.01}_{-0.02}$	0.14 (f)	$0.15^{+0.06}_{-0.01}$	0.15 (f)	keV
compTT-1	τ	$12.4^{+2.1}_{-1.4}$	$20.2^{+4.0}_{-4.9}$	20.2 (f)	$13.8^{+3.4}_{-3.8}$	13.8 (f)	
compTT-1	$norm$	$1.67^{+1.22}_{-0.94}$	$0.52^{+2.31}_{-0.22}$	$0.56^{+0.02}_{-0.02}$	$4.51^{+4.61}_{-2.40}$	$4.69^{+0.34}_{-0.34}$	
compTT-2	T_0	–	compTT-1- kT	compTT-1- kT	$0.14^{+0.03}_{-0.04}$	0.14 (f)	KeV
compTT-2	kT	–	$0.33^{+0.10}_{-0.11}$	0.33 (f)	$1.98^{+\infty}_{-1.65}$	1.98 (f)	keV
compTT-2	τ	–	$12.5^{+11.7}_{-2.5}$	12.5 (f)	$2.71^{+9.69}_{-2.52}$	2.71 (f)	
compTT-2	$norm$	–	$7.67^{+7.82}_{-2.88} \times 10^{-3}$	$8.42^{+0.41}_{-0.41} \times 10^{-3}$	$0.88^{+7.78}_{-0.78} \times 10^{-3}$	$1.01^{+0.06}_{-0.06} \times 10^{-3}$	
nthComp	kT_e	200 (f)	keV				
nthComp	kT_{bb}	compTT-1- kT	compTT-2- kT	compTT-2- kT	$0.12^{+0.24}_{-0.12}$	0.12 (f)	keV
nthComp	Γ	$2.20^{+0.04}_{-0.04}$	$2.11^{+0.05}_{-0.05}$	2.11 (f)	$2.05^{+0.08}_{-0.05}$	2.05 (f)	
nthComp	$norm$	$3.93^{+0.40}_{-0.39} \times 10^{-4}$	$2.11^{+1.34}_{-0.72} \times 10^{-4}$	$2.04^{+0.05}_{-0.05} \times 10^{-4}$	$3.45^{+0.68}_{-1.84} \times 10^{-4}$	$3.29^{+0.10}_{-0.10} \times 10^{-4}$	
χ^2/dof		704.4/653	653.2/646	585.3/573	647.8/644	579.5/571	

Table 2. The contributions of various spectral components to the variability spectra, as indicated by the percentage of normalization relative to the components in the time-averaged spectra for the best-fit Model-2.

	QPO Rms (%)	QPO Cov (%)	HF Rms (%)	LF Rms (%)	LF Cov (%)
<i>Figure 5: Obs-9 Spectra</i>					
diskbb	$9.1^{+2.4}_{-1.2}$	$8.4^{+1.7}_{-1.1}$	$0.0^{+4.9}_{-0.8}$	$0.0^{+2.4}_{-0.4}$	$0.0^{+2.5}_{-0.4}$
compTT-1	0.0	0.0	$3.7^{+0.8}_{-0.8}$	$10.2^{+0.4}_{-0.4}$	$9.3^{+0.5}_{-0.5}$
compTT-2	$18.8^{+3.6}_{-3.6}$	$17.3^{+1.9}_{-1.9}$	$7.6^{+2.9}_{-2.9}$	$0.0^{+3.4}_{-0.0}$	$0.0^{+2.8}_{-0.0}$
nthComp	$11.6^{+2.6}_{-2.6}$	$10.7^{+1.7}_{-1.6}$	$19.6^{+2.0}_{-2.0}$	$15.0^{+1.5}_{-1.5}$	$3.9^{+1.8}_{-1.8}$
<i>Figure 7: Obs-2 Spectra</i>					
diskbb	$0.0^{+0.8}_{-0.0}$	$0.0^{+0.8}_{-0.0}$	$0.0^{+3.6}_{-0.0}$	$0.0^{+3.7}_{-0.0}$	$0.0^{+3.2}_{-0.0}$
compTT-1	$0.0^{+0.4}_{-0.0}$	$0.0^{+0.4}_{-0.0}$	$2.9^{+0.7}_{-0.7}$	$8.5^{+0.5}_{-0.5}$	$7.4^{+0.6}_{-0.6}$
compTT-2	$17.0^{+3.3}_{-3.3}$	$15.9^{+1.4}_{-1.4}$	$4.2^{+2.4}_{-2.4}$	$3.9^{+1.9}_{-1.9}$	$5.3^{+2.2}_{-2.2}$
nthComp	$10.4^{+2.3}_{-2.3}$	$9.8^{+1.4}_{-1.4}$	$10.7^{+1.8}_{-1.8}$	$13.0^{+1.5}_{-1.5}$	$5.8^{+1.8}_{-1.8}$

trum, and so its effect on the lag spectrum can be ignored. We only consider the lag between compTT-1 and nthComp, which is signified by $t_{\text{lag},1}$. The intrinsic light curve of compTT is assumed to be the light curve in 0.4-0.6 keV, because this band is dominated by compTT in Model-1. Likewise, the 2-10 keV light curve is used to represent nthComp. The adoption of these observed light curves avoids potential problems of introducing unrealistic light curves from simulations. Then it is necessary to force the two light curves to have the required lag of $t_{\text{lag},1}$ in the QPO frequency bin of $(2.5-3.5) \times 10^{-4}$ Hz. To achieve this we perform Fourier transform on the light curve of compTT, and then modify the phase in the QPO frequency bin to introduce the required lag of $t_{\text{lag},1}$ relative to nthComp. Then we perform inverse Fourier transform to derive a new light curve for compTT, whose QPO phase leads nthComp by $t_{\text{lag},1}$.

As the first attempt (Model-1-T1), we fix $t_{\text{lag},1}$ at -861 s,

which is the observed lag between 0.3-0.35 keV and 2-10 keV, as shown in Figure 2c. The minus sign indicates the soft X-ray lead. Then the lag is calculated for different energy bins between 0.3 and 10 keV. Comparing this with the observed lag spectrum, the χ^2 is 666.4 for 9 dof, so clearly it is a very poor fit. Then we set $t_{\text{lag},1}$ as a free parameter (Model-1-T2), and fit the lag spectrum. Now the best-fit $t_{\text{lag},1}$ is found to be -337 ± 23 s, with the χ^2 being 137.0 for 8 dof, so it remains as a poor fit, as shown by the blue solid line in Figure 6. Therefore, we conclude that the best-fit Model-1 cannot reproduce the observed lag spectrum.

We now examine the spectral decomposition of Model-2. The QPO’s rms and covariance spectra can be fit by using diskbb, compTT-2 and nthComp. Thus we introduce two lag variables. $t_{\text{lag},1}$ signifies the lag between diskbb and nthComp, and $t_{\text{lag},2}$ signifies the lag between compTT-2 and nthComp. Following the spectral decomposition of Model-2, we adopt the light curve in the 0.3-0.35 keV band for diskbb, 0.85-1 keV for compTT-2, and 2-10 keV for nthComp. These light curves are manipulated in the same way so as to provide the required lag of $t_{\text{lag},1}$ and $t_{\text{lag},2}$.

We first attempt to fit a single lag (Model-2-T1), with $t_{\text{lag},2}$ being fixed at 0 s, i.e. assuming that there is no lag time between compTT-2 and nthComp. The resultant best-fit $t_{\text{lag},1}$ is found to be -877 ± 47 s, and the χ^2 is 33.8 for 8 dof, indicating a much better fit than Model-1. However, as shown by the red dash line in Figure 6, this lag model cannot reproduce the lag spectrum in 0.6-2 keV. Now we allow both $t_{\text{lag},1}$ and $t_{\text{lag},2}$ to be free parameters (Model-2-T2). This produces a very good fit to the lag spectrum, with the χ^2 being 4.9 for 7 dof, as shown by the red solid line in Figure 6. The best-fit $t_{\text{lag},1}$ is -859 ± 50 s, and $t_{\text{lag},2}$ is -180 ± 34 s. In summary, the QPO’s lag spectrum requires diskbb to lead compTT-2 by 679 s, and requires compTT-2 to lead nthComp by 180 s. Based on the simplest constraint of causality in time, we can speculate that the QPO is created

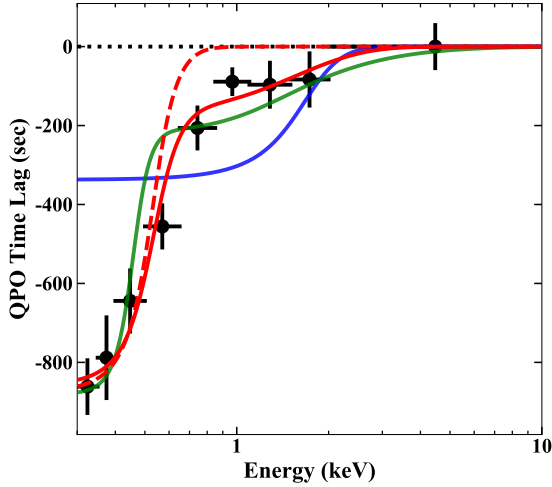


Figure 6. Modelling the QPO’s lag spectrum. The data are shifted down by 421 s to allow the data point in the 2–10 keV band to be at zero. The blue solid, red dash, red solid and green solid lines represent the results for the Model-1-T2, Model-2-T1, Model-2-T2, Model-2b-T2 in Table 3, respectively.

in `diskbb`. It then propagates to `compTT-2` and `nthComp`, and it is also amplified during this process.

Finally, we check if the spectral decomposition of Model-2b can also fit the QPO’s lag spectrum. In this spectral decomposition, if we fix $t_{\text{lag},2}$ at 0 s (Model-2b-T1), the best-fit $t_{\text{lag},1}$ is found to be 905 ± 54 s, but this is clearly a bad fit, as shown by the large χ^2 of 82.1 for 8 dof (see Table 3). If we allow both time lags to be free parameters (Model-2b-T2), then $t_{\text{lag},1}$ and $t_{\text{lag},2}$ are found to be -882 ± 56 s and -307 ± 40 s. The resultant χ^2 is 22.9 for 7 dof, which is worse than Model-2-T2. As shown by the green solid line in Figure 6, the main problem with Model-2b-T2 is that its `diskbb` has a too low temperature.

Consequently, we conclude that the QPO’s lag spectrum indicates that Model-2 provides a better spectral decomposition than Model-2b and Model-1. The best-fit spectral components derived from the combined spectral-timing analysis (Model-2) can also fit the independent data from the QPO’s lag spectrum. This demonstrates that this model can capture all the spectral variability information, and that the complexity of an additional soft Compton component (`CompTT-2`) is required by the data.

4.3 Constraining the Potential Presence of a Reflection Component

The iron $K\alpha$ line is a typical feature present in an X-ray reflection spectrum. This line is generally weak or undetected in ‘X-ray simple’ super-Eddington NLS1s (Gallo 2006), while the ‘X-ray complex’ NLS1s have a different story (Done & Jin 2016). There has been a long and continuing debate about the cause of this weakness in ‘X-ray simple’ NLS1s, with suggestions including an intrinsically weak reflection component, or reflection which is so highly smeared so as to form only a continuum. However, recent studies are pointing to the former (a weak reflection) possibility (e.g. Jin, Done & Ward 2016; Kara et al. 2017; Parker, Miller & Fabian

Table 3. Results of fitting the QPO’s lag spectrum. Model-1-T1 and Model-1-T2 are based on the best-fit Model-1, where $t_{\text{lag},1}$ is the time lag between `compTT` and `nthComp`. Model-2-T1 and Model-2-T2 are based on the best-fit Model-2, where $t_{\text{lag},1}$ is the time lag between `diskbb` and `nthComp`, and $t_{\text{lag},2}$ is the time lag between `compTT-2` and `nthComp`. Model-2b-T1 and Model-2b-T2 are based on the best-fit Model-2b. ‘f’ indicates that this parameter is fixed. All the error bars indicate 1σ uncertainties.

Model	$t_{\text{lag},1}$ (sec)	$t_{\text{lag},2}$ (sec)	χ^2/dof
Model-1-T1	-861 (f)	–	666.4/9
Model-1-T2	-337 ± 23	–	137.0/8
Model-2-T1	-877 ± 47	0 (f)	33.8/8
Model-2-T2	-859 ± 50	-180 ± 34	4.9/7
Model-2b-T1	-905 ± 54	0 (f)	82.1/8
Model-2b-T2	-882 ± 56	-307 ± 40	22.9/7

2018). An Iron $K\alpha$ line feature has never been detected in RE J1034+396, but the limits are not very constraining due to the low S/N above 4 keV. Our 72 ks *XMM-Newton* observation in Obs-9 provides a similar spectral quality as previous observations, but for the first time the simultaneous 100 ks *NuSTAR* exposure provides much better spectral quality above 3 keV. Thus now we can combine the *XMM-Newton* and *NuSTAR* data to constrain a potential underlying reflection component. In order to maximize the spectral constraints we also add the two MOS spectra, as well as the entire set of variability spectra.

We now consider Model-2 as the continuum model, and add a reflection component to it by convolving `nthComp` with the reflection model `rfxconv` (Done & Gierliński 2006; Kolehmainen, Done & Díaz Trigo 2011). The key parameters of `rfxconv` include the relative reflection normalization (R_{refl}^3) and the ionization parameter in logarithm ($\log\xi$). The inclination angle is fixed at 30° , and the iron abundance is fixed at the Solar value. The `kdblur` model (Laor 1991) is then multiplied to the reflection component to account for the relativistic smearing. The emissivity index of `kdblur` is fixed at its default value of 3, the outer radius is fixed at $100 R_g$, and the inclination angle is fixed at 30° . The inner radius (R_{in}) remains as a free parameter.

Figure 8 shows the best-fit result with a minimal χ^2 of 1074.5 for 1032 dof. The reflection component is found to be very weak. Comparing this to the best-fit Model-2 without reflection, the improvement of χ^2 is only 8.6 for 7 additional free parameters, and so the improvement of fitting is not statistically significant. We note that the main contributor to the χ^2 ’s improvement is the high S/N time-averaged spectrum from the EPIC-pn alone, which is 8.5 for 3 dof, corresponding to a slightly higher significance of 2.1σ . The best-fit R_{refl} is $0.20^{+0.16}_{-0.11}$, indicating that at most the reflecting material occupies less than 40% of the sky as seen from the X-ray source. The constraint placed on R_{refl} comes mainly from the spectra above 5 keV, driven both by the lack of the $K\alpha$ emission line and the Compton hump. The best-fit $\log\xi$ is $3.06^{+0.21}_{-0.21}$, so the reflecting gas is very

³ In the `rfxconv` model, R_{refl} is actually a negative value in order to show the reflection component only. The upper limit of the iron abundance parameter A_{iron} is 3.

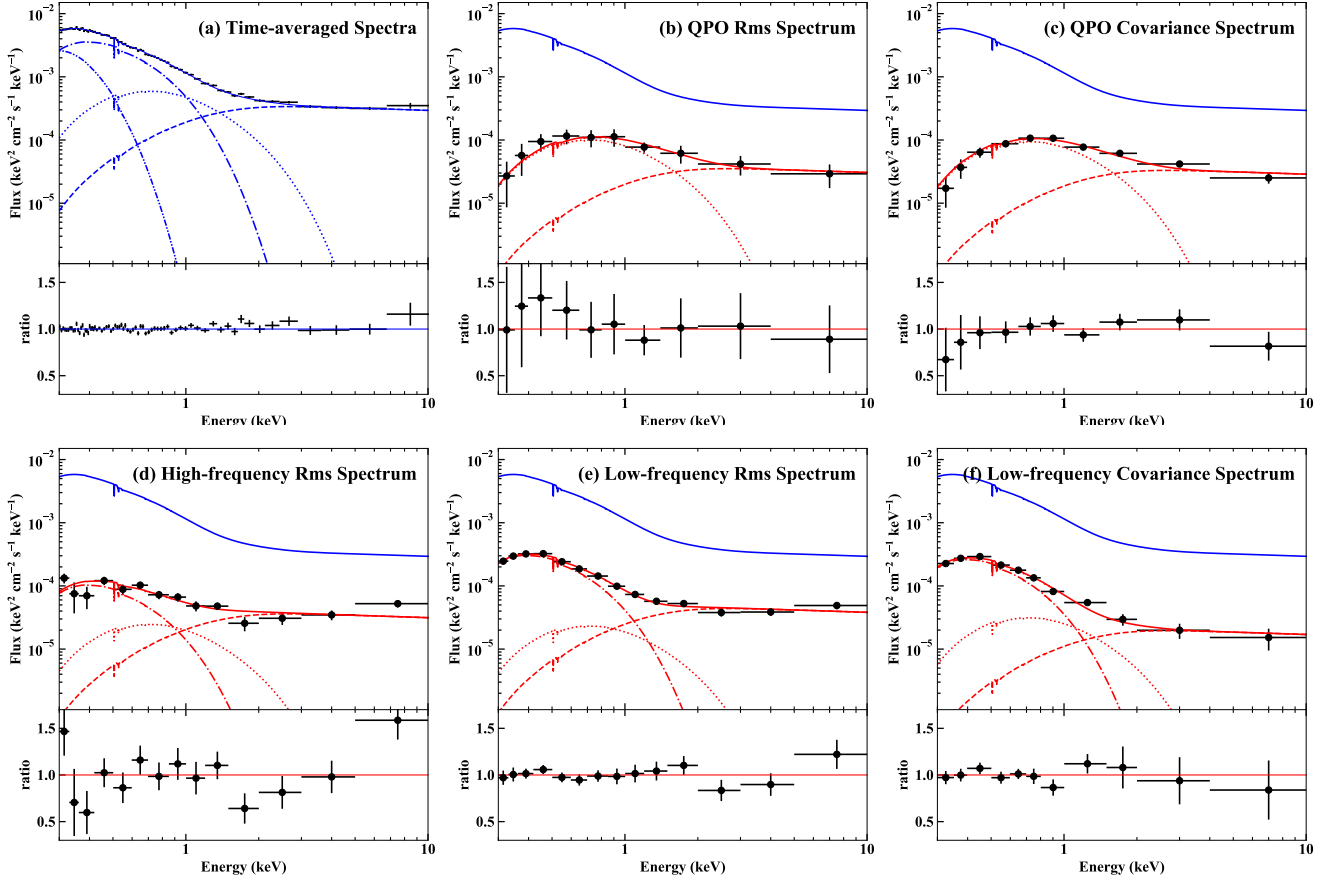


Figure 7. Similar to Figure 5, but now applying the best-fit Model-2 of Obs-9 to the same set of spectra from Obs-2. Only the intrinsic absorption and the normalizations of spectral components are allowed to vary, while the shape of every component remains the same. This model also produces good fits to Obs-2.

highly ionized, and the line is intrinsically broadened. The best-fit R_{in} is found to be $4.18^{+8.42}_{-2.57}$. Thus although the spin cannot be directly constrained, nevertheless the result is still consistent with a low-spin black hole.

In order to examine the degeneracy of model parameters, we perform a Markov Chain Monte Carlo (MCMC) sampling of the parameter space using the XSPEC-EMCEE program⁴. Figure 9 shows the level of degeneracy among R_{in} , R_{refl} and $\log\xi$. It is clear that R_{refl} and $\log\xi$ are somewhat correlated, with a smaller R_{refl} allowed for smaller $\log\xi$. This is understandable because if the material is less ionized, the emission lines in the reflection component will appear stronger and narrower, so the reflection fraction R_{refl} must decrease in order to maintain a good fit to the smooth spectra. Actually, if we examine Figure 8 closely, it can be noticed that the *NuSTAR*/FPMB spectrum does not show any line feature in the Iron $K\alpha$ line's band, although the spectral resolution and S/N are not sufficient to provide a useful statistically significant constraint.

The iron abundance (A_{iron}) is also a sensitive parameter because it strongly influences the intensity of the Iron $K\alpha$

feature in the model. We also try to set A_{iron} as a free parameter, and find that the χ^2 only decreases by 1.2 for 1 more free parameter, and A_{iron} is found to be $2.84^{+0.16}_{-0.44}$, indicating a super-solar iron abundance³. In addition, R_{refl} decreases to $0.15^{+0.08}_{-0.08}$, and $\log\xi$ remains at a large value of $3.30^{+0.39}_{-0.16}$. Since relaxing A_{iron} does not result in a significant improvement to the fit, but does increase the parameter degeneracy, we no longer consider it in this work. Future observations with deeper exposures are required to place stronger constraints on the underlying reflection and $K\alpha$ emission feature in RE J1034+396.

5 COMPARISONS WITH PREVIOUS OBSERVATIONS

5.1 Fitting the Spectra from Obs-2

We now return to the previous data and see whether the new spectral decomposition of Model-2 can provide us with any additional insights into the longer-term behaviour of the QPO in this source. Obs-2 is the first *XMM-Newton* observation of RE J1034+396 showing a significant QPO (Gierliński et al. 2008). It is also the only data set whose quality allows us to extract a similar set of variability spectra. We present a careful analysis of the pile-up effect in Obs-2, and ensure that

⁴ The XSPEC-EMCEE program is developed by Jeremy Sanders, which makes use of the EMCEE package (Foreman-Mackey et al. 2013).

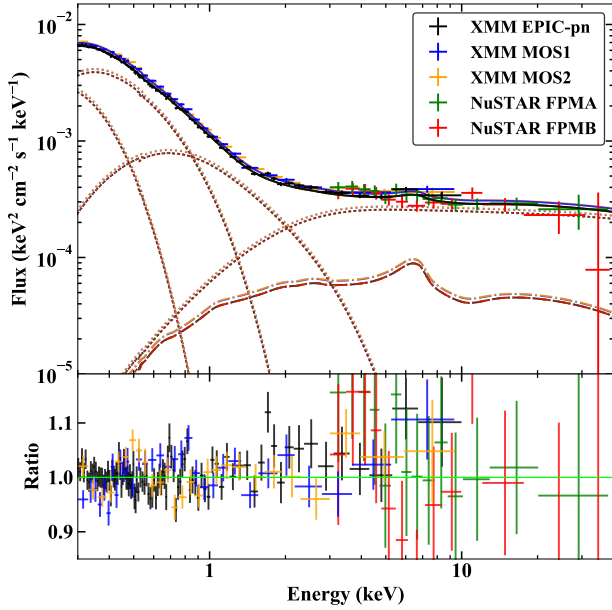


Figure 8. Constraining the potential reflection component using all the spectra available in Obs-9. The dotted lines correspond to the four continuum components in Model-2 as shown in Figure 5a. Dash-dotted lines indicate the best-fit reflection component in every spectrum.

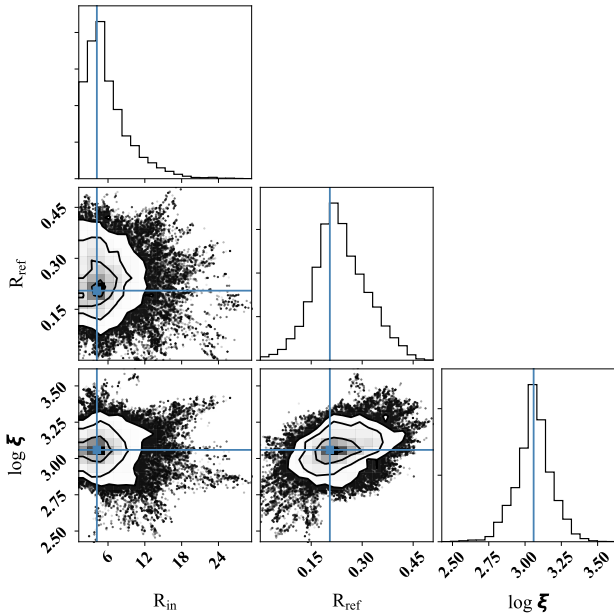


Figure 9. Posterior probability distributions of the inner radius R_{in} of the relativistic blurring (`kdblur`), the relative reflection normalization R_{ref} and the ionization parameter $\log \xi$ of the reflection component, and their covariances derived from the MCMC sampling. Their best-fit values are indicated by the blue solid lines.

it does not affect the results presented in this paper⁵. Then we use the spectra from Obs-2 to verify the best-fit Model-2 and Model-2b from Obs-9. Since there is no simultaneous *NuSTAR* observation for Obs-2, the time-averaged spectrum is only available within 0.3–10 keV by *XMM-Newton*. We assume that the spectra from Obs-2 have the same components as in Obs-9, and the shape of each component is kept the same, only their normalizations are allowed to vary. The intrinsic absorption ($N_{H,host}$) is also treated as a free parameter. Then we fit all the time-averaged and variability spectra of Obs-2, simultaneously.

For Model-2 the overall minimal χ^2 is found to be 585.3 for 573 dof, indicating reasonably good fits to all the spectra. The best-fit $N_{H,host}$ is found to be $2.59^{+0.63}_{-0.65} \times 10^{20} \text{ cm}^{-2}$, which is slightly higher than that in Obs-9. The spectral decomposition of the time-averaged spectrum is shown in Figure 7a, which is very similar to Obs-9. The QPO’s rms and covariance spectra are well fit by `compTT-2` and `nthComp`, as shown in Panels-b and c. The HF rms, LF rms and covariance spectra all require contributions from `compTT-1`, `compTT-2` and `nthComp`. We also apply the best-fit Model-2b to the spectra from Obs-2, and the resultant χ^2 is 579.5 for 571 dof, which represents an improvement of 1.9σ significance comparing to Model-2. Hence the results are very similar between Model-2b and Model-2.

Comparing the fitting results between Obs-9 and Obs-2, we find that there are subtle differences in the spectrum of the stochastic noise components around 1 keV between Obs-2 and Obs-9, and there is a major difference in the QPO spectrum below 0.5 keV. In terms of the components, the main difference in the QPO is that the `diskbb` component is present in Obs-9 but not in Obs-2. Otherwise the rest of the QPO is similarly well fit by the same combination of `compTT-2` and `nthComp` in Obs-2 as in Obs-9. However, `compTT-2` is stronger in the HF rms spectra of Obs-2 than in Obs-9, and is also present in the LF rms and covariance spectra in Obs-2. These results provide important clues for our understanding of the physical origins of these components, which we discuss in more detail in Section 8.1.

5.2 Fitting the Spectra from the non-QPO Obs-3 and Obs-6

Amongst all of the 9 *XMM-Newton* observations of RE J1034+396, Obs-3 and 6 are the only two observations in which the QPO signal was not detected even with a good enough data quality (Alston et al. 2014). These two observations were carried out by *XMM-Newton* on 2009-05-31 and 2011-05-07 separately. Interestingly, RE J1034+396 shows a much stronger soft excess during these two observations than during the other observations, and so it appears that there is an anti-correlation between the intensity of the soft excess and the QPO’s detectability (Paper-I). We test if this different spectral state in Obs-3 and 6 can also be fitted by the same spectral components in the best-fit Model-2. Similarly, we only allow $N_{H,ins}$ and the normalization of every spectral component to be free parameters.

Figure 10 shows the best-fit results for these two observations. The overall minimal χ^2 for Obs-3 and 6 is 778.0

⁵ see Appendix B

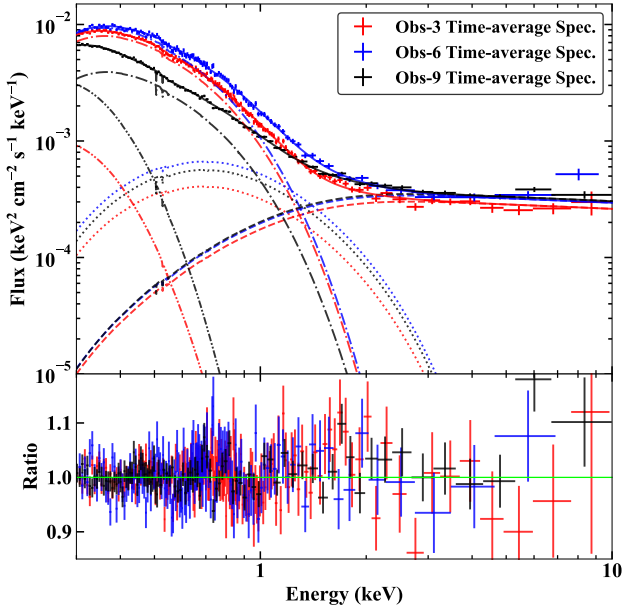


Figure 10. Applying the best-fit Model-2 of Obs-9 to the time-average spectra in Obs-3 and 6 when the QPO is not detected. The black, red and blue spectra are the time-averaged spectra from Obs-9, 3 and 6, respectively. The dash-dot lines represent the non-QPO `compTT-1` component, which have caused the much stronger soft excesses in Obs-3 and 6.

for 746 dof, indicating reasonably good fits to both spectra. The best-fit $N_{\text{H,host}}$ is $0.97^{+0.84}_{-0.78} \times 10^{20} \text{ cm}^{-2}$ for Obs-3 and $1.09^{+0.83}_{-0.11} \times 10^{20} \text{ cm}^{-2}$ for Obs-6. If we tie the normalization of `diskbb` between Obs-3 and Obs-6, the best-fit χ^2 only increases by 1.0, equivalent to 1σ significance. If we set the normalizations of all the components to be the same between Obs-3 and 6, except $N_{\text{H,ins}}$ and an overall normalization factor, then the best-fit χ^2 increases by 10.8 for a reduction of 3 dof, equivalent to 2.5σ significance. Thus the shape difference between the time-averaged spectra in Obs-3 and Obs-6 is not significant, mainly the overall flux of Obs-6 is a factor of 1.27 ± 0.02 higher than for Obs-3.

The most remarkable difference is the enhancement of `compTT-1` in the two non-QPO observations, as also shown in Figure 10. In comparison with the time-averaged spectra in Obs-9, `compTT-1` is a factor of $1.97^{+0.05}_{-0.10}$ stronger in Obs-3, and a factor of $2.35^{+0.09}_{-0.13}$ stronger in Obs-6. Interestingly, `compTT-1` is also the only spectral component that is not required by the QPO spectra in Obs-2 and 9. Therefore, `compTT-1` is very likely to be the main driver for the anti-correlation between the intensity of the soft excess and the QPO's detectability as reported in Paper-I.

However, we also note that the increase of the flux of `compTT-1` in Obs-3 and 6 is not enough to dilute the QPO signal across the entire 0.3–10 keV band. Thus the disappearance of the QPO is not a simple flux-dilution effect. In other words, if the QPO were present at the same strength in `compTT` as in Obs-9, then there would be sufficient S/N to detect it in Obs-3 and 6. Therefore, the enhancement of `compTT-1` must instead indicate a physical change in the accretion flow into a state which does not produce a QPO.

Table 4. The best-fit parameters of two broadband SEDs for RE J1034+396 in Obs-9. ‘f’ indicates that this parameter is fixed. For linked parameters, we put the parameter names in the table instead of values. Default values are adopted for all the model parameters not listed here.

Comp.	Par.	SED-1	SED-2	Unit
TBabs	$N_{\text{H,gal}}$	1.36 (f)	1.36 (f)	10^{20} cm^{-2}
zTBabs	$N_{\text{H,host}}$	$2.64^{+0.65}_{-0.97}$	$0.59^{+0.42}_{-0.43}$	10^{20} cm^{-2}
redden	$E_{\text{B-V,gal}}$	1.34 (f)	1.34 (f)	10^{-2}
zredden	$E_{\text{B-V,host}}$	$= N_{\text{H,host}} \times 1.7 \times 10^{-22}$		
agnsed	M_{BH}	$1.68^{+0.05}_{-0.25}$	$11.83^{+1.64}_{-4.09}$	$10^6 M_{\odot}$
agnsed	$\log(\dot{m})$	$0.43^{+0.08}_{-0.07}$	$-0.70^{+0.19}_{-0.06}$	
agnsed	a_*	$0.26^{+0.04}_{-0.03}$	$0.97^{+0.01}_{-0.07}$	
agnsed	$kT_{\text{e,warm}}$	$0.21^{+0.03}_{-0.02}$	$0.23^{+0.02}_{-0.02}$	keV
agnsed	$kT_{\text{e,hot}}$	100 (f)	100 (f)	keV
agnsed	Γ_{hot}	$2.19^{+0.04}_{-0.05}$	$2.16^{+0.04}_{-0.04}$	
agnsed	Γ_{warm}	$3.34^{+0.16}_{-0.14}$	$3.43^{+0.12}_{-0.13}$	
agnsed	R_{hot}	$6.0^{+1.0}_{-0.9}$	$2.08^{+0.85}_{-0.36}$	R_{g}
agnsed	R_{warm}	$10.2^{+2.3}_{-0.3}$	$131.8^{+143.5}_{-60.0}$	R_{g}
hostgal	norm	$0.33^{+0.03}_{-0.03}$	$0.28^{+0.03}_{-0.03}$	
const		$1.04^{+0.04}_{-0.04}$	$1.05^{+0.03}_{-0.04}$	
χ^2/dof		634.3/596	633.8/596	

6 MULTI-WAVELENGTH PROPERTIES

6.1 Broadband Spectral Energy Distribution Modelling

In these sections we explore how the QPO properties depend on the wider multi-wavelength properties of the AGN. In steady state models the accretion flow has constant mass accretion rate at all radii. Thus the optical/UV emission from the outer accretion disc can be used to determine the accretion rate through the X-ray emitting inner regions once the black hole mass is known (e.g. Davis & Laor 2011, Done et al. 2012), modulo corrections for spin and inclination. Since there is very little host galaxy absorption, or even much warm absorption, it seems most likely that RE J1034+396 is close to face on. The host galaxy is similarly face on (with a bar, see *HST* image⁶).

To build the spectral energy distribution (SED) extending down to the optical/UV, we use the UVOT data from the simultaneous *Swift* ToO observation. This provides multi-band photometry (UVW2, UVM2, UVW1, U, B, V) to support the *XMM-Newton*/OM data which was taken in UVW1 fast mode only to search for fast variability. These data, together with the *XMM-Newton*/EPIC and *NuSTAR* spectra, allow us to build the best simultaneous broadband SED of RE J1034+396.

We fit this with the latest *XSPEC* model for the accretion flow continuum, `agnsed` (Kubota & Done 2018). This model is based on the physical concept described above, that the mass accretion rate is constant with radius and the radial emissivity corresponds to that of a thin disc (Novikov-Thorne) but that the emission mechanism changes from that of a blackbody to warm Comptonisation at R_{warm} , and from warm Comptonisation to hot Comptonisation at R_{hot} . This is an refinement of the `optxagnf` model (Done et al. 2012),

⁶ <http://archive.stsci.edu/cgi-bin/mastpreview?mission=hst&dataid=JD95120>

which uses the more sophisticated passive disc scenario for the warm Comptonisation (Petrucci et al. 2018), and calculates the temperature of seed photons of the hot Comptonisation internally. The model only includes a single temperature warm Comptonisation region, rather than the two temperature model preferred by all the spectral-timing results, but we focus first on the overall energetics rather than the detailed soft X-ray shape.

We fix the electron temperature of the hot corona at its default value of 100 keV⁷. The disc outer radius is chosen to be the self-gravity radius calculated inside the model using Laor & Netzer (1989). The inclination angle is taken to be 30°. Since it is known that the host galaxy star light contributes significantly to the optical emission of RE J1034+396 (Bian & Huang 2010; Czerny et al. 2016), we use the spectral template of an Sb galaxy from Polletta et al. (2007) to model it, incorporated as the local `hostgal` model. Galactic absorption is considered in the same way as in previous X-ray analysis. The Galactic dust reddening⁸ is modelled by the `zredden` model with $E_{B-V,gal}$ being fixed at 0.0134 for the light-of-sight of RE J1034+396 (Schlegel, Finkbeiner & Davis 1998). Dust reddening from the host galaxy ($E_{B-V,host}$) is assumed to be $1.7 \times 10^{-22} N_{H,host}$ (Bessell 1991). Based on the cosmology model noted in Section 1, we adopt a co-moving distance of 175.2 Mpc for RE J1034+396 (Wright 2006). A free constant is included in the model to account for any potential calibration differences between the normalizations of *XMM-Newton*/OM and *Swift*/UVOT.

After performing the SED fitting in XSPEC, we find a range of local minima in χ^2 depending on black hole mass/spin. These span from low mass, low spin solutions, where the standard disc extends down into the lowest energy end of the *XMM-Newton*/EPIC bandpass, and the warm Comptonisation only fills in between this and the hot Comptonisation (SED-1), up to the highest mass, highest spin solution where most of the UV and soft X-ray emission is produced by the warm Comptonisation, with the standard disc component only contributing to the optical emission (SED-2).

Both SEDs-1 and 2 provide comparably good fits to all the data (see Table 4), but the black hole mass in SED-1 is consistent with the values derived from independent mass estimators such as the H β line velocity width (Czerny et al. 2016). We therefore prefer SED-1, with the low black hole mass of $1.68^{+0.05}_{-0.25} \times 10^6 M_{\odot}$, the black hole spin is also low at $a_* = 0.26^{+0.04}_{-0.24}$, and the mass accretion rate through the outer disc (\dot{m}) is high at $2.69^{+0.54}_{-0.40}$. This is marginally super-Eddington, though not sufficiently extreme for advection of radiation to produce a large change in the predicted SED (Kubota & Done 2019). We note that `agnsed` does not include the combined effects of red and blue-shifts expected from the fast orbital velocities of gas under the influence of strong gravity. Although these effects are not so large for low spin solutions (see e.g. Done et al. 2013).

As an additional check, we also seek to replace the `agnsed` model by the `agnslim` model (Kubota & Done 2019).

`agnslim` has a similar set of parameters, but it also takes into account the suppressed radiative efficiency in the inner disc region due to the strong advection and/or disk wind operating in the super-Eddington state. The best-fit results of `agnslim` are found to be very similar to `agnsed`, with the former having a slightly larger χ^2 of 636.9 for 597 dof. This result confirms that since RE J1034+396 is only slightly super-Eddington, the additional effects of super-Eddington accretion state do not introduce significant differences to the SED model.

The decomposition of SED-1 in the X-ray band is similar to the best-fit Model-1 in that there is a standard disc component at the lowest energies, but we have previously shown that Model-2 gives a better solution for the X-ray spectral variability of RE J1034+396. Therefore, we refit the unfolded X-ray spectrum of SED-1 with the three Comptonisation components of Model-2. Unsurprisingly, a good fit can be achieved because the unfolded spectra from Model-1 and Model-2 are very similar (see Figure 4a and Figure 5a). The reason of adopting this approach is to retain energy conservation between the disc and corona in SED-1. Figure 11 shows the best-fit SED, where the two Comptonisation components in SED-1 have now been replaced by the three Comptonisation components in Model-2. We present this result as the so-far best physical SED decomposition for RE J1034+396. The optical emission is dominated by starlight from the host galaxy, the UV bump is dominated by emission from the outer accretion disc, and the X-ray emission is from the inner disc and also the three Comptonisation regions.

6.2 Exploring the UV Variability

Figure 11 also shows that the UVW1 filter of OM is dominated by the accretion disc emission, and so it tracks the mass accretion rate through the outer disc. We can explore the short-term UV variability by extracting the light curve in the UVW1 filter in Obs-9, which is shown in Figure 12a. No intrinsic rms can be found in this UV band, nor does there exist any UV/X-ray correlation, as indicated by the Pearson's correlation coefficient of -0.05. We also examine the cross-correlation function between the UV and X-ray light curves, and find no significant lagged correlation. Therefore, we can conclude that the UV variability is much weaker than the X-rays. This is very similar to that observed in several other super-Eddington NLS1s such as RX J0439.6-5311, whose optical/UV emission is also dominated by the disc emission, and no intrinsic UV variability is detected in this band (Jin et al. 2017b). But this is in contrast to some AGN with much lower Eddington ratios such as NGC 5548, where significant variability is observed in the UV/optical band, which is also correlated with the X-rays because of X-ray reprocessing (e.g. Edelson et al. 2015; Gardner & Done 2017).

Since all the 9 *XMM-Newton* observations of RE J1034+396 have simultaneous ultraviolet observations in UVW1, we can construct a long-term light curve in UVW1. This begins with the first X-ray observation in 2002, through to the latest observation in 2018, as is shown in Figure 13. This light curve shows the variation of \dot{m} though the outer disc of RE J1034+396 during the past 16 years. Specifically, the two observations showing no QPO signal are Obs-3 and

⁷ This parameter has very little effect on the SED fitting. We also try to fix it at 200 keV, the difference in the resultant χ^2 is only 0.1, and the best-fit parameters hardly change.

⁸ <https://irsa.ipac.caltech.edu/applications/DUST>

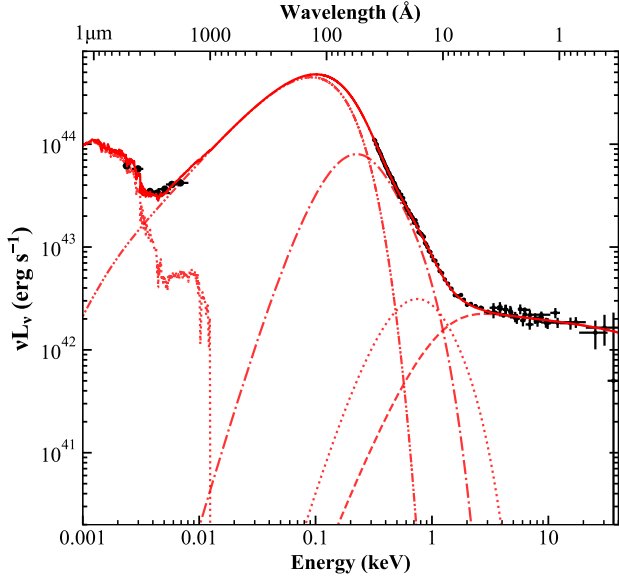


Figure 11. The best-fit broadband SED of RE J1034+396 in Obs-9. The multi-wavelength data comprise the *Swift* UVOT and *XMM-Newton* OM data in optical/UV, the *XMM-Newton* EPIC-pn spectrum in 0.3-10 keV and the *NuSTAR* FPMA/FPMB spectra in 3.0-40 keV. This SED is based on the best-fit SED-1, but the two Comptonisation components have been replaced by the three Comptonisation components in Model-2. The red solid line shows the entire best-fit SED. The red dotted lines in the optical/IR shows the best-fit host galaxy component. The red dash-dot-dot, dash-dot, dotted, and dash lines represent the best-fit accretion disc component in SED-1, the *compTT-1*, *compTT-2* and *nthComp* components in Model-2, respectively.

6, which have the lowest and highest \dot{m} , respectively. Therefore, we can exclude \dot{m} as the direct trigger of the X-ray QPO, although a delayed influence cannot be ruled out due to poor sampling of this long-term light curve.

7 ANALOGY OF SPECTRAL-TIMING PROPERTIES BETWEEN RE J1034+396 AND GRS 1915+105

GRS 1915+105 is a famous Galactic black hole binary (BHB) with a super-Eddington luminosity and a low-temperature Comptonisation component (Done, Wardziński & Gierliński 2004; Middleton et al. 2006). During its disc-dominated spectral state, a high-frequency QPO at ~ 67 Hz is sometimes observed, with a quality factor of ~ 20 (Morgan, Remillard & Greiner 1997). The peak frequency of this QPO varies between 65 and 72 Hz, and its rms amplitude increases from 1 per cent at a few keV to 11 per cent at 40 keV (Belloni & Altamirano 2013; Belloni et al. 2019). Previous studies have shown that the QPO frequency seen in RE J1034+396 is consistent with a simple mass scaling factor of the 67 Hz QPO in GRS 1915+105, and that their X-ray spectra are similarly dominated by a soft component (Middleton et al. 2009; Middleton & Done 2010; Czerny et al. 2016). These two QPOs also have similar quality factors and small variation of peak frequency (Paper-I).

However, a key failure in this analogy is the soft X-ray lag seen in the QPO spectrum of Obs-2 (e.g. Zoghbi &

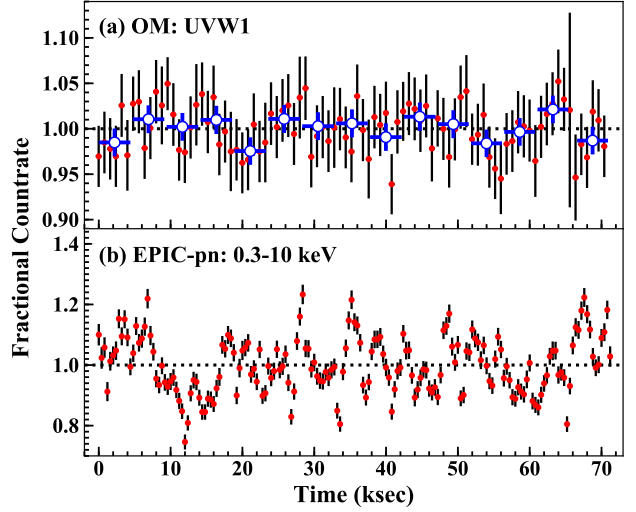


Figure 12. Panel-a: the OM fast-mode light curve (800 s binned) in the UVW1 filter in Obs-9, as shown by the red points. The blue points show photometric fluxes derived from the simultaneous imaging-mode exposures. Panel-b: the simultaneous EPIC-pn light curve (400 s binned) in 0.3-10 keV plotted for comparison. There is no significant correlation between the two light curves (Pearson’s correlation coefficient is -0.05). The intrinsic rms of the UVW1 light curve is also consistent with zero.

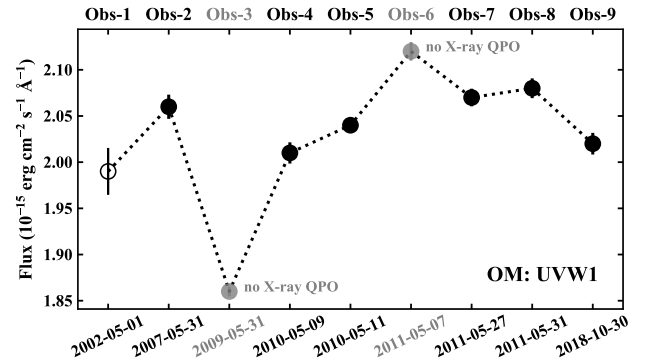


Figure 13. The long-term UV light curve of RE J1034+396 as observed by *XMM-Newton*/OM in the UVW1 filter. Six observations show the X-ray QPO (black points), two observations do not show the QPO (grey points), one observation does not have sufficient data quality for the QPO analysis (open circle point). No correlation is found between the UV flux and the QPO’s detectability.

Fabian 2011), which is the opposite to the soft X-ray lead seen in GRS 1915+105 (Méndez et al. 2013). However, this issue is now resolved, because we showed in Paper-I that the new data clearly show a soft X-ray lead for the stronger QPO detection in Obs-9. However, another difference is that so-far no harmonics have been found for the QPO in RE J1034+396 (Alston et al. 2014; Paper-I), whereas they have been detected in GRS 1915+105, but only in some observations (e.g. Belloni, Méndez & Sánchez-Fernández 2001; Strohmayer 2001; Remillard et al. 2002). Thus this particular difference may not be such a serious issue.

Here we use the stronger QPO of Obs-9 to explore the

link to the 67 Hz QPO in GRS 1915+105 in more detail, with a direct comparison of the spectral-timing properties between RE J1034+396 and GRS 1915+105. We take the rms spectrum of the 67 Hz QPO from Fig. 6 in Belloni & Altamirano (2013), and take its phase lag spectrum from Fig. 4 in Méndez et al. (2013). Both of these two studies use the *RXTE* data of GRS 1915+105 taken in 21th Oct. 2003 (OBSID: 80701-01-28-00, 01, 02). The frequency of the QPO in RE J1034+396 Obs-9 is 3550 s, implying a factor of 2.38×10^5 between this and GRS 1915+105, consistent with a mass of $3 \times 10^6 M_{\odot}$ for RE J1034+396 assuming $12.4 M_{\odot}$ for GRS 1915+105 (Reid et al. 2014).

Disc temperatures scale as $T^4 \propto \dot{m}/M$, so if these two black hole systems have similar Eddington ratios, then their disc temperatures should be a factor ~ 20 different (see also Middleton et al. 2009). The *RXTE* spectra of GRS 1915+105 from 3-40 keV, scaled down by a factor of 20, serendipitously matches very well to the *XMM-Newton* energy range for RE J1034+396. We apply this shifting factor, and compare the rms variability and phase lag from these two objects directly (Figure 14 Panels-a and b). It is clear that the QPO of RE J1034+396 and the 67 Hz QPO of GRS 1915+105 are indeed very similar in terms of both their rms and lag spectra.

We extract the time-averaged spectra of GRS 1915+105 from the above *RXTE* datasets, and create an absolute rms spectrum for the 67 Hz QPO. These spectra are fitted with the four spectral components in the Model-2 configuration. Figure 14c shows the best-fit results. Note that the `nthComp` component is poorly constrained due to the poor S/N at high energies, so we simply fix its slope at 2.0, and set its normalization as the same between the time-averaged spectrum and rms spectrum. Since the two sources have very different black hole masses, it is not correct to directly compare their model parameters. But generally speaking, this spectral decomposition of GRS 1915+105 is similar to RE J1034+396 (see Figure 5a). The most noticeable point is that the `compTT-1` component does not appear in the 67 Hz QPO's rms spectrum, either.

Finally, we compare the unfolded, unabsorbed and time-averaged spectra between the two sources in a phenomenological way, which is shown in Figure 14d, where again we shift the energy of GRS 1915+105 down by a factor of 20 in order to match the energy range of RE J1034+396. For the ease of comparison, the flux is shifted down by a factor of 1000. This flux scaling factor is somewhat expected. Since the energy shifting factor is 20, the disc luminosity should roughly scale down by a factor of 20^4 . Then the flux also scales with D^{-2} where D is the source distance. Adopting the luminosity distance of $D_R = 182.6$ Mpc for RE J1034+396 and $D_G = 8.6$ kpc for GRS 1915+105 (Reid et al. 2014), the shifting factor for the flux is $20^4 \times (D_G/D_R)^2 \simeq 3.5 \times 10^{-4}$. The remaining factor of ~ 3 can be attributed to the much larger inclination angle of GRS 1915+105 than RE J1034+396.

Surprisingly, the spectra shown in Figure 14d are somewhat different: the soft excess of RE J1034+396 is weaker than in GRS 1915+105, but its hard X-ray tail is much stronger. In particular the spectrum of GRS 1915+105 has the convex curvature which is more like that seen in the non-QPO observations of RE J1034+396 (blue points).

However, this might also be related to the different inclination angles between GRS 1915+105 and RE J1034+396. GRS 1915+105 is at a moderate inclination angle, where

the Doppler boost from the high velocity inner disc offsets its gravitational redshift, whereas RE J1034+396 is much more likely to be face on, so gravitational redshifts dominate. We note that the `agnsed` model used for SED-1 does not include these effects. There is also the possibility of black hole spin but this is rather uncertain in both objects. As we discuss above, we prefer the low mass which is also low spin solution of SED-1 for RE J1034+396, but we note that the stronger redshifts expected for a face on disc could allow a higher spin solution, while in GRS 1915+105 there are different spin values claimed for different assumed electron temperature of the `nthcomp` component (Middleton et al. 2006; Remillard & McClintock 2006).

8 DISCUSSION

8.1 Relationship between the Soft Excess and QPO

Soft X-ray excess is a ubiquitous feature of the majority of the bright AGN population, but an X-ray QPO is a rather rare phenomenon, detected in less than ten AGN so far, and only in RE J1034+396 with both high significance and repeatability. Thus RE J1034+396 provides us with a unique laboratory in which to investigate the relationship between the soft excess and the presence of a QPO. It is clear from Paper-I and previous studies that the QPO is strongly associated with the shape of the soft X-ray spectrum in RE J1034+396, where the QPO is quenched when the soft X-ray spectrum is stronger, and has a more convex (thermal-looking) shape.

Our latest Obs-9 data with the strongest and most coherent AGN QPO ever seen, allows us to explore the various energy-dependent variability properties of this QPO and the stochastic variability both at low and high frequencies (although the latter has more limited statistics). Our analysis favor a model in which the QPO traces the hottest part of the soft X-ray excess emission, while the stochastic variability links to a cooler component. We also show that the previous datasets from RE J1034+396 can also be well fit with this model, although in Obs-9 the QPO is also very strong at the lowest energies (which we interpret as part of the `diskbb` component), which is not the case in Obs-2.

The QPO in RE J1034+396 is so long lasting that it must be a fundamental frequency of the system itself rather than just some transient 'hot spot' or occultation event. It is probably analogous to the 67 Hz QPO observed in GRS 1915+105 as the frequencies scale in mass, and here we show that the 67 Hz QPO is likewise associated with the hottest part of the strong soft X-ray emission in GRS 1915+105. It seems that there is a region at the inner edge of the accretion flow which is radially distinct enough that it exhibits particular spectral and variability behaviours.

The `agnsed` spectral models have distinct radial regions, with the high energy hot Comptonisation from $R_{isco} - R_{hot}$ and the warm Comptonisation(s) from $R_{hot} - R_{warm}$. In this model, the warm Comptonisation is associated with the optically thick, geometrically thin(ish) accretion disc, while the hot component is part of an optically thin(ish), geometrically thick accretion flow. Coherent oscillations are easier to excite and maintain when the radial region is small. This

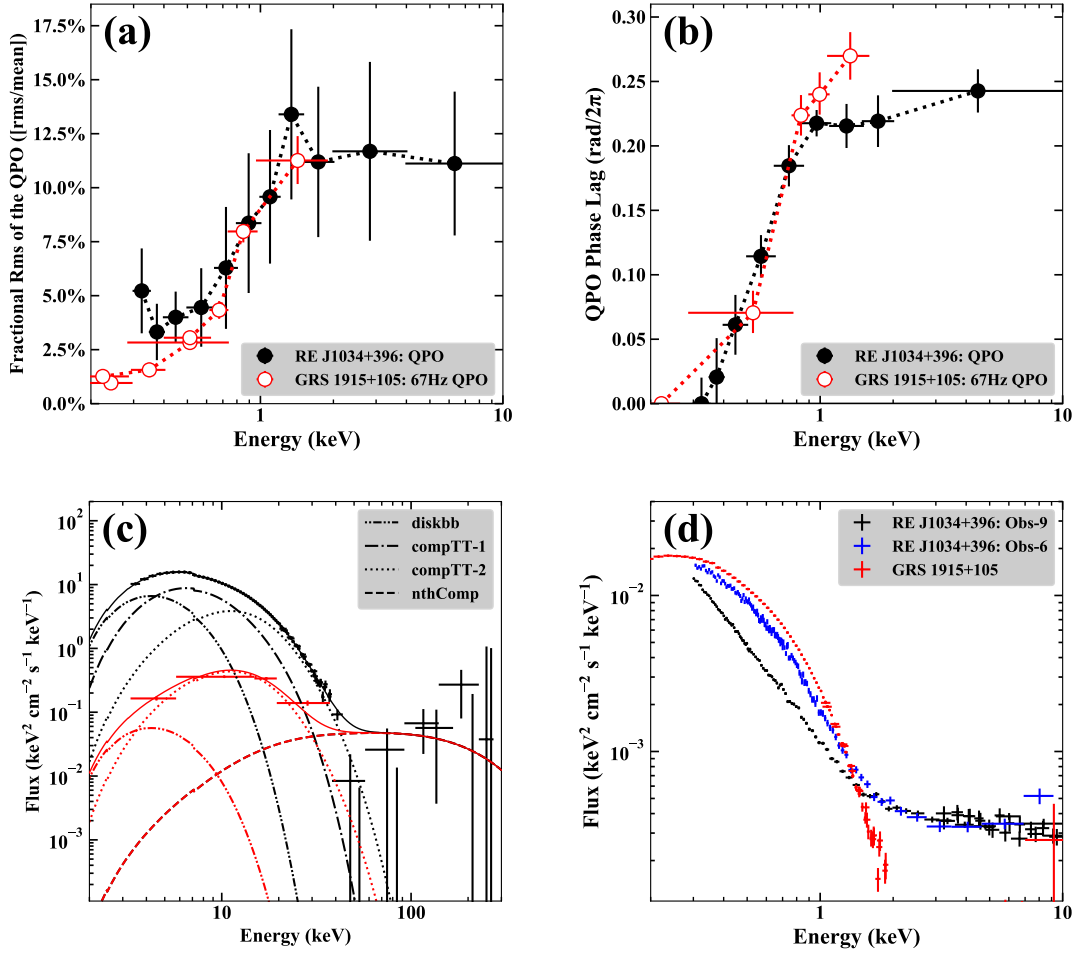


Figure 14. Comparison of spectral-timing properties between RE J1034+396 and GRS 1915+105. Panels-a and b: comparisons for the QPO’s rms and phase lag spectra between RE J1034+396 in Obs-9 and GRS 1915+105 (67 Hz QPO, shifted down by a factor of 20 in energy). The rms and phase lag spectra for the 67 Hz QPO of GRS 1915+105 are obtained from Fig.4a in Méndez et al. (2013) and Fig.6 in Belloni et al. (2013), separately. Panel-c: applying a similar model to the *RXTE* spectra of GRS 1915+105 during its 67 Hz QPO observations (OBSID: 80701-01-28-00, 01, 02). The rms spectrum of the 67 Hz QPO is shown in red. Panel-d: comparison of unfolded and unabsorbed spectra between RE J1034+396 during Obs-9 (with a QPO) and Obs-6 (without a QPO), and GRS 1915+105 being shifted down by a factor of 20 in energy and 1000 in flux.

occurs when the source is close to the Eddington limit for the hot Comptonisation, and maybe for the warm Comptonisation region as well (Kubota & Done 2018). Both RE J1034+396 and GRS 1915+105 show that it is the hottest part of the warm Comptonisation region which is oscillating most strongly, so we are observing a small radial region at the edge of a geometrically thin(ish) disc.

There are multiple oscillation modes which can exist for a narrow, thin disc ring, from purely geometric displacements such as a vertical or radial offset about an equilibrium position centred on some radius r_0 , with width dr_0 , on the equatorial plane at $z_0 = 0$. However, pressure forces within the disc should be important, which can be incorporated in models of slender (or non-slender) tori. These have an internal vertical structure, with elliptical cross-section centred on $r_0, z_0 = 0$, but now with height dz_0 at r_0 , tapering down to 0 at $r_0 \pm dr_0$. These tori have the geometric displacement modes in radius and vertical height as before, but also have modes which affect the vertical structure. The ‘breathing’

mode changes dz_0 without changing dr_0 , the ‘plus’ mode is an anti-correlated increase in dz_0 with decreasing dr_0 , and the ‘X’ mode is an anti-correlated increase in z_0 at $r_0 + dr_0$ with a decrease at $r_0 - dr_0$. Intrinsically, the proper area of the torus does not change for a vertical or ‘X’ mode, whereas it does for the radial, ‘plus’ and ‘breathing’ modes. Vincent et al. (2014) show the power generated by the changing position and/or shape of this torus assuming constant emissivity per unit (proper) area when folded through a fully general relativistic (GR) spacetime. The GR effects amplify the power in vertical changes at high inclination, and this, coupled to the real change in emitting area of the ‘breathing’ mode, make this the strongest power spectral feature in their simulations at 85° . While GRS 1915+105 is at moderately high inclination, RE J1034+396 is most probably face on, where this ‘breathing’ mode has much less power than the ‘plus’ mode.

The similarity of the (phase) lags in the QPO in both RE J1034+396 and GRS 1915+105 argues for this being

the same type of oscillation in each case, so we prefer the association of both QPOs with the ‘plus’ mode.

However, none of these simulations allow for a real change in heating/cooling rate, and hence the real change in temperature and emissivity which will accompany such oscillations. This has been explored only for the much lower frequency Lense-Thirring (relativistic vertical precession) mode, which is a purely geometric mode but where the changing angle of the torus with respect to the disc results in changing the flux of seed photons intercepted to cool the flow (You, Bursa & Zycki 2018). In addition, the expansion/compression of the torus in the ‘breathing’ and ‘plus’ modes could also give rise to intrinsic changes in cooling/heating rates. The two warm Comptonisation components in our analysis could then instead be associated with the unperturbed torus `compTT-1`, whereas the additional heating/cooling in the QPO modulation gives the additional contribution to the QPO from `compTT-2` and (sometimes) `diskbb`.

9 CONCLUSIONS

This paper builds on and extends the results of Paper-I of the re-detection of the QPO in Obs-9. Here we use these data to examine the QPO in more detail, using the combined spectral-timing techniques as well as the full multi-wavelength data in the simultaneous *XMM-Newton*, *NuSTAR* and *Swift* observations. These results provide new insights on the relationship between the soft excess and the QPO, and reinforce the QPO’s analogy with the 67 Hz QPO detected in the Galactic micro-quasar GRS 1915+105. We summarize the main results below.

- we present the detailed energy dependence of the QPO’s timing properties, including its peak frequency, rms, phase lag and coherence. Steep increases of rms and lag (i.e. soft X-ray lead) are observed from 0.3 to 1 keV, and both of them flatten towards harder X-rays, with the maximal rms being 12.4% and lag being 861 s (equivalent to a 0.24 phase lag).
- we extract the rms, coherence and lag spectra for the LF and HF bands outside the QPO frequency bin. Both HF and LF rms spectra increase from 0.3 to 10 keV, although an extra hump is observed at LF below 1 keV. No significant covariance is found between soft and hard X-rays for these stochastic variabilities. A tentative time lag of ~ 1000 is noticed below 0.4 keV at the frequency band below 10^{-4} Hz.
- we fit the *XMM-Newton* and *NuSTAR* time-averaged spectra and the 5 types of variability spectra simultaneously with different models. We find that four spectral components are needed, including a disc component (`diskbb`), two warm Comptonisation components (`compTT-1`, `compTT-2`) and a hot Comptonisation component (`nthComp`), in order to produce good fits to all the spectra. Our results indicate that `compTT-1` exhibits strong stochastic variability, while the QPO is concentrated in the hotter, less luminous `compTT-2`. This model can also fit the QPO lag spectrum very well, with `diskbb` leading `compTT-2` by 679 s, which in turn leading `nthComp` by 180 s.

- the best-fit Model-2 components can also produce good fits to the spectra from Obs-2, 3 and 6, without changing the shape of each component. The main difference in Obs-2 is that the hotter `compTT-2` QPO component also contains some stochastic variability. Conversely, in the non-QPO observations of Obs-3 and 6, the main difference is that the cooler `compTT-1` component is much stronger.
- we construct the optical to hard X-ray broadband SED of RE J1034+396 with the state-of-the-art models. We find that the QPO’s detectability is not directly correlated with the mass accretion rate through the outer disc as traced by the UV flux. No short-term UV variability is detected by *XMM-Newton*/OM.
- using the simultaneous *XMM-Newton* and *NuSTAR* spectra, we constrain the underlying reflection component to be less than 20% in the hard X-rays, and there is no significant detection of the iron $K\alpha$ line,
- we show that the rms and phase lag spectra between the QPO of RE J1034+396 and the 67 Hz QPO of GRS 1915+105 are very similar. The four components in Model-2 can also decompose the time-averaged spectra and QPO’s rms spectrum of GRS 1915+105 in a similar way after shifting the energy scale for the mass difference, although the curvature of the soft excess is slightly different. This may be due to the difference in inclination between these two sources.

We emphasize the importance of having more data to verify the association of the QPO with the highest temperature part of the soft X-ray excess, as well as more sensitive high energy observations to better constrain the QPO in the 2-10 keV range, and especially any iron line/reflection signature. Our speculation associating the QPO with the ‘plus’ mode of an overheated inner edge of the disc predicts that the warm Comptonisation region pulsation is seen as seed photons by the hot Compton region, so this seed photon modulation should propagate into the hot Comptonisation on the light travel time. Since we measure this at 180 s, this implies a distance of $\sim (18 - 12) R_g$ for a black hole mass of $(2 - 3) \times 10^6 M_\odot$.

However, the faintness of the source above 2 keV means that while deeper *XMM-Newton* observations will help, a full picture may only emerge from future studies with the large effective area of missions such as *Athena*. The next generation X-ray all sky monitor such as *Einstein Probe* can also observe RE J1034+396 regularly, and thus can monitor its long-term spectral evolution and its anti-correlation with the QPO’s detectability, and even help to constrain the duty cycle of the QPO’s presence.

ACKNOWLEDGEMENTS

We thank the *Swift* team for approving and conducting the target-of-opportunity observations. CJ thanks Jiren Liu for helpful discussions on the line features. CD thanks Frederic Vincent and Chris Fragile for useful discussions about the torus modes, and especially acknowledges the beautiful movies from Frederic Vincent of the ray traced simulations. CJ acknowledges the National Natural Science Foundation of China through grant 11873054, as well as the support by the Strategic Pioneer Program on Space Science, Chi-

nese Academy of Sciences through grant XDA15052100. CD and MJW acknowledge the Science and Technology Facilities Council (STFC) through grant ST/P000541/1 for support.

This work is based on observations conducted by *XMM-Newton*, an ESA science mission with instruments and contributions directly funded by ESA Member States and the USA (NASA). This work also made use of data from the *NuSTAR* mission, a project led by the California Institute of Technology, managed by the Jet Propulsion Laboratory, and funded by the National Aeronautics and Space Administration. This research has made use of the NASA/IPAC Extragalactic Database (NED) which is operated by the Jet Propulsion Laboratory, California Institute of Technology, under contract with the National Aeronautics and Space Administration.

REFERENCES

- Alston W. N., Done C., Vaughan S., 2014, *MNRAS*, 439, 1548
 Arévalo P., Uttley P., 2006, *MNRAS*, 367, 801
 Arnaud K. A., 1996, *ASPC*, 101, 17
 Arnaud K. A., et al., 1985, *MNRAS*, 217, 105
 Ballantyne D. R., Ross R. R., Fabian A. C., 2001, *MNRAS*, 327, 10
 Belloni T. M., Altamirano D., 2013, *MNRAS*, 432, 10
 Belloni T., Hasinger G., 1990, *A&A*, 230, 103
 Belloni T., Méndez M., Sánchez-Fernández C., 2001, *A&A*, 372, 551
 Belloni T. M., Bhattacharya D., Caccese P., Bhlerao V., Vadawale S., Yadav J. S., 2019, *MNRAS*, 489, 1037
 Bessell M. S., 1991, *A&A*, 242, L17
 Bian W. H., Huang K., 2010, *MNRAS*, 401, 507
 Blackburn J. K., 1995, *ASPC*, 77, 367, *ASPC...77*
 Boller T., Brandt W. N., Fink H., *A&A*, 305, 53
 Boroson T. A., 2002, *ApJ*, 565, 78
 Crummy J., Fabian A. C., Gallo L., Ross R. R., 2006, *ApJ*, 365, 1067
 Czerny B., et al., 2016, *A&A*, 594, A102
 Davis S. W., Laor A., 2011, *ApJ*, 728, 98
 Done C., Davis S. W., Jin C., Blaes O., Ward M., 2012, *MNRAS*, 420, 1848
 Done C., Gierliński M., 2006, *MNRAS*, 367, 659
 Done C., Jin C., 2016, *MNRAS*, 460, 1716
 Done C., Jin C., Middleton M., Ward M., 2013, *MNRAS*, 434, 1955
 Done C., Wardziński G., Gierliński M., 2004, *MNRAS*, 349, 393
 Edelson R., et al., 2015, *ApJ*, 806, 129
 Emmanoulopoulos D., McHardy I. M., Papadakis I. E., 2011, *MNRAS*, 416, L94
 Fabian A. C., et al., 2009, *Nature*, 459, 540
 Foreman-Mackey D., Hogg D. W., Lang D., Goodman J., 2013, *PASP*, 125, 306
 Gallo L. C., 2006, *MNRAS*, 368, 479
 Gardner E., Done C., 2017, *MNRAS*, 470, 3591
 Gardner E., Done C., 2014, *MNRAS*, 442, 2456
 Gierliński M., Done C., 2004, *MNRAS*, 349, L7
 Gierliński M., Middleton M., Ward M., Done C., 2008, *Nature*, 455, 369
 Harrison F. A., et al., 2013, *ApJ*, 770, 103
 Hu C.-P., Chou Y., Wu M. C., Yang T. C., Su Y. H., 2011, *ApJ*, 740, 67
 Huang N. E., et al., 1998, *RSPSA*, 454, 903
 Jansen F., Lumb D., Altieri B., et al., 2001, *A&A*, 365, L1
 Jin C., Done C., Ward M., 2020, *MNRAS*, 495, 3538 (Paper-I)
 Jin C., Done C., Ward M., 2017a, *MNRAS*, 468, 3663
 Jin C., Done C., Ward M., 2017b, *MNRAS*, 471, 706
 Jin C., Done C., Ward M., 2016, *MNRAS*, 455, 691
 Jin C., Done C., Middleton M., Ward M., 2013, *MNRAS*, 436, 3173
 Jin C., Ward M., Done C., Gelbord J., 2012a, *MNRAS*, 420, 1825
 Jin C., Ward M., Done C., 2012b, *MNRAS*, 422, 3268
 Jin C., Ward M., Done C., 2012c, *MNRAS*, 425, 907
 Jin C., Done C., Ward M., Gierliński M., Mullaney J., 2009, *MNRAS*, 398, L16
 Kara E., Alston W. N., Fabian A. C., Cackett E. M., Uttley P., Reynolds C. S., Zoghbi A., 2016, *MNRAS*, 462, 511
 Kara E., García J. A., Lohfink A., Fabian A. C., Reynolds C. S., Tombesi F., Wilkins D. R., 2017, *MNRAS*, 468, 3489
 Kolehmainen M., Done C., Díaz Trigo M., 2011, *MNRAS*, 416, 311
 Kotov O., Churazov E., Gilfanov M., 2001, *MNRAS*, 327, 799
 Kubota A., Done C., 2019, *MNRAS*, 489, 524
 Kubota A., Done C., 2018, *MNRAS*, 480, 1247
 Kubota A., Done C., 2004, *MNRAS*, 353, 980
 Kubota A., Makishima K., Ebisawa K., 2001, *ApJL*, 560, L147
 Laor A., 1991, *ApJ*, 376, 90
 Laor A., Netzer H., 1989, *MNRAS*, 238, 897
 Maitra D., Miller J. M., 2010, *ApJ*, 718, 551
 Méndez M., Altamirano D., Belloni T., Sanna A., 2013, *MNRAS*, 435, 2132
 Middleton M., Done C., 2010, *MNRAS*, 403, 9
 Middleton M., Done C., Ward M., Gierliński M., Schurch N., 2009, *MNRAS*, 394, 250
 Middleton M., Done C., Gierliński M., Davis S. W., 2006, *MNRAS*, 373, 1004
 Middleton M., Uttley P., Done C., 2011, *MNRAS*, 417, 250
 Morgan E. H., Remillard R. A., Greiner J., 1997, *ApJ*, 482, 993
 Page K. L., Schartel N., Turner M. J. L., O'Brien P. T., 2004, *MNRAS*, 352, 523
 Parker M. L., Miller J. M., Fabian A. C., 2018, *MNRAS*, 474, 1538
 Petrucci P.-O., et al., 2018, *A&A*, 611, A59
 Polletta M., et al., 2007, *ApJ*, 663, 81
 Porquet D., Reeves J. N., O'Brien P., Brinkmann W., 2004, *A&A*, 422, 85
 Puchnarewicz E. M., Mason K. O., Siemiginowska A., Pounds K. A., 1995, *MNRAS*, 276, 20
 Reid M. J., McClintock J. E., Steiner J. F., Steeghs D., Remillard R. A., Dhawan V., Narayan R., 2014, *ApJ*, 796, 2
 Remillard R. A., McClintock J. E., 2006, *ARA&A*, 44, 49
 Remillard R. A., Munro M. P., McClintock J. E., Orosz J. A., 2002, *ApJ*, 580, 1030
 Ross R. R., Fabian A. C., 1993, *MNRAS*, 261, 74
 Schlegel D. J., Finkbeiner D. P., Davis M., 1998, *ApJ*, 500, 525
 Strohmayer T. E., 2001, *ApJL*, 554, L169
 Titarchuk L., 1994, *ApJ*, 434, 570
 Turner T. J., Pounds K. A., 1988, *MNRAS*, 232, 463
 Uttley P., Cackett E. M., Fabian A. C., Kara E., Wilkins D. R., 2014, *A&ARv*, 22, 72
 Verner D. A., Ferland G. J., Korista K. T., Yakovlev D. G., 1996, *ApJ*, 465, 487
 Vincent F. H., Mazur G. P., Straub O., Abramowicz M. A., Kluźniak W., Török G., Bakala P., 2014, *A&A*, 563, A109
 Wilkinson T., Uttley P., 2009, *MNRAS*, 397, 666
 Wilms J., Allen A., McCray R., 2000, *ApJ*, 542, 914
 Wright E. L., 2006, *PASP*, 118, 1711
 Wu, Z., Huang, N. E. 2009, *AADA*, 1, 1
 You B., Bursa A., Życki P. T., 2018, *ApJ*, 858, 82
 Zdziarski A. A., Johnson W. N., Magdziarz P., 1996, *MNRAS*, 283, 193
 Zoghbi A., Reynolds C., Cackett E. M., Miniutti G., Kara E., Fabian A. C., 2013, *ApJ*, 767, 121

APPENDIX A: SEARCHING FOR SOFT X-RAY ABSORPTION LINES

The soft X-ray spectrum of RE J1034+396 was reported to contain a few absorption lines, which are produced by partially ionized oxygen, neon and iron elements (Middleton, Uttley & Done 2011). It was also reported that an extra absorption feature appears during the QPO trough at 0.86 keV, which is interpreted as the O VIII K-edge at its theoretical energy of 0.87 keV (i.e. 0.84 keV in the observer's frame, Maitra & Miller 2010). This absorption feature was proposed to be evidence for the existence of a warm absorber, whose variability is correlated with the QPO. The location of this warm absorber was estimated to be $\sim 15 R_g$ from the central black hole, and the QPO can be explained as periodic obscuration by this ionized material. However, Middleton, Uttley & Done (2011) analyzed the RGS spectrum of Obs-2, and argued that the small radius of this absorber is in contradiction with the low turbulence and outflow velocities as measured from the RGS spectra.

Since the absorption lines are claimed to be related to the QPO, we also search for soft X-ray absorption features in the RGS spectra whose spectral resolution is higher than EPIC cameras. Since the significance of line feature is directly related to the continuum, we use the spectral components in the best-fit Model-2 (see Section 4.1.2) to fit the continua of RGS spectra, and use narrow Gaussian components to fit potential absorption lines.

Figure A1 shows the RGS spectra relative to their best-fit continua for both Obs-2 and 9. The rest frame energies of various potential features are marked, but plainly there is nothing which is highly significant. A feature consistent with 0.923 keV can be seen in all spectra. However, its significance is not straightforward to determine precisely due to the 'look elsewhere' effect, from the number of independent energies searched. Nonetheless, since this has been claimed before, we use a standard $\Delta\chi^2 = 9$ for a 3σ significance. This gives 3.3σ in Obs-2 and 4.3σ in Obs-9. If we assume this line is a blue-shifted O VIII K-edge, then the velocity along the line-of-sight would be as large as $\sim 0.048c$ (c is the speed of light). Then the line should appear broad either because of strong turbulence or the velocity distribution of the outflowing material, which is not observed in the spectrum, so we rule out the origin of O VIII K-edge, and attribute it to the closer Fe XIX (0.919 keV) line. We also identify other absorption lines such as O VIII and Fe XVIII in both Obs-2 and 9, although their significances are all less than 3σ (see Table A1).

In order to check if these absorption lines correlate with the QPO phase (Maitra & Miller 2010) or continuum flux, we perform QPO phase-resolved spectroscopy and 0.3-10 keV flux-resolved spectroscopy using the EPIC-pn data in Obs-2 and 9, with a similar method as described in Maitra & Miller (2010). Our approach is to use the intrinsic mode function (IMF) at the QPO's timescale to identify local peaks and troughs of the QPO, which is derived by applying the Ensemble Empirical Mode Decomposition (EEMD) method to the 0.3-10 keV light curve (Huang et al. 1998; Wu & Huang 2009; Hu et al. 2011; Paper-I). We define the time and flux at every QPO extremum as $[T_{\min}, F_{\min}]$ for every QPO trough, and $[T_{\max}, F_{\max}]$ for every QPO peak. Then each of the interval between the consecutive pair of extrema, i.e.

Table A1. Soft X-ray absorption lines detected in the RGS spectrum. The listed parameters are for the best-fit Gaussian profile. Negative line velocities indicate outflows. The last column indicates the detection significance.

Absorption Line	Obs	$E_{\text{line, res}}$ (keV)	v_{line} (c)	EW (eV)	Sig. (σ)
Fe XIX (0.919 keV)	Obs-2	0.923	0.004	-3.9	3.3
	Obs-9	0.924	0.006	-5.4	4.3
Fe XVIII (0.773 keV)	Obs-2	0.780	0.009	-0.8	1.5
	Obs-9	0.785	0.016	-1.1	1.1
O VIII (0.655 keV)	Obs-2	0.656	0.002	-1.2	3.1
	Obs-9	0.655	0.001	-0.6	1.7

$[T_{\min}, T_{\max}]$ or $[T_{\max}, T_{\min}]$, is divided into three sub-intervals. We use the factor μ to define the flux within the interval as $F_{\min} + \mu(F_{\max} - F_{\min})$, thus the value of μ is within (0,1). The three sub-intervals are defined for $\mu = (0, 0.3)$, $(0.3, 0.7)$, $(0.7, 1)$, and are referred to as low phase (LP), intermediate phase (IP) and high phase (HP), respectively. For the flux-resolve spectra, we define four flux ranges, which are 0-5.0, 5.0-5.7, 5.7-6.5 and >6.5 counts s^{-1} for Obs-2 and 0-5.0, 5.0-5.7, 5.7-6.5 and >6.5 counts s^{-1} for Obs-9, and these flux ranges are signified by Flux-1 to 4. Similarly, the spectral components in Model-2 are used to fit the continuum in these spectra. Potential absorption lines are fitted with Gaussian components.

However, we cannot detect a broad O VIII K-edge in any of the spectra derived above in either Obs-2 or 9. This is most likely because our continuum model is more sophisticated, and the spectral quality of the new Obs-9 dataset is better. The narrow Fe XIX absorption line can be detected. Table A2 compares the significance of Fe XIX absorption line in different spectra. Despite the low significance of detection, we notice that the Fe XIX line appears most significant in the QPO-LP spectra in both Obs-2 and 9, and so it is possible that this line is correlated with the QPO phase. If this correlation is caused by the response of ionization state to the changing illumination as proposed by Maitra & Miller (2010), then it should show an even stronger correlation with the flux state. However, the significances of this line in the flux-resolve spectra are all much smaller than in the QPO-LP spectrum, thus the illumination scenario can be ruled out, unless the obscuring material only 'sees' the variation of QPO but not the continuum flux, which is difficult to explain. However, this potential correlation between the Fe XIX line and QPO phase is still too vague, but we encourage to explore it in more detail with future observations.

APPENDIX B: INFLUENCE OF THE PILE-UP EFFECT ON THE VARIABILITY SPECTRA IN OBS-2

A potential issue associated with Obs-2 is the pile-up effect, because EPIC-pn was in the full-frame mode, and the pile-up threshold is below the count-rate of RE J1034+396. In paper-I we have determined that in order to safely remove the pile-up effect, the central 10 arcsec of the point-spread-function (PSF) should be excised. This inner radius is slightly larger than the 7.5 arcsec radius which was adopted

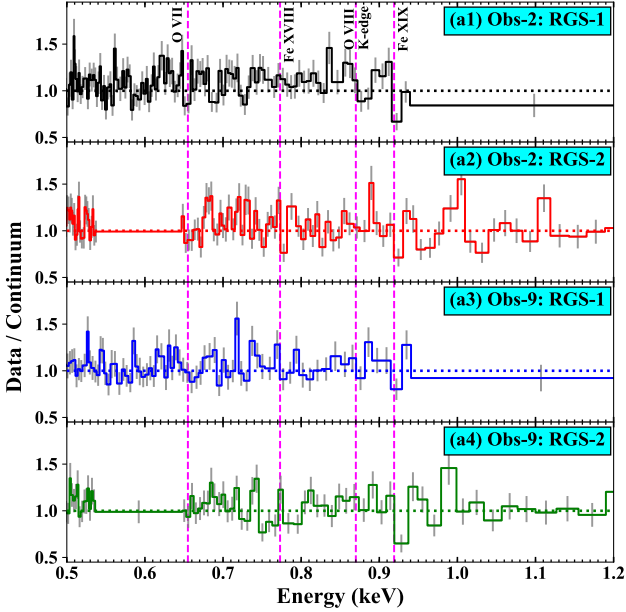


Figure A1. The RGS spectra of RE J1034+396 observed in Obs-2 and 9. These are shown as the ratio between the data and the best-fit continuum model. The positions of some important absorption lines are marked by the vertical dash lines at their energies in the AGN’s rest-frame. Note that the O VIII K-edge is not detected.

Table A2. Best-fit parameters by fitting a Gaussian profile to the Fe XIX (rest frame: 0.919 keV) absorption line in the QPO phase-resolved spectra and 0.3-10 keV flux-resolved spectra. QPO-HP, MP and LF indicate the high-phase, medium-phase and low-phase. Flux-1 to 4 indicate the sequence from the highest flux to the lowest.

Obs	Spectrum	$E_{\text{line, res}}$ (keV)	EW (eV)	Significance (σ)
Obs-2	QPO-HP	0.920 ($v_{\text{line}} = 0.001c$)	-0.0	0.0
Obs-2	QPO-MP	tied to QPO-HP	-1.0	0.3
Obs-2	QPO-LP	tied to QPO-HP	-5.1	1.8
Obs-9	QPO-HP	0.938 ($v_{\text{line}} = 0.02c$)	-0.0	0.0
Obs-9	QPO-MP	tied to QPO-HP	-0.4	0.1
Obs-9	QPO-LP	tied to QPO-HP	-8.0	3.1
Obs-2	Flux-1	0.971 ($v_{\text{line}} = 0.06c$)	-2.8	0.6
Obs-2	Flux-2	tied to Flux-1	-5.4	1.7
Obs-2	Flux-3	tied to Flux-1	-0.0	0.0
Obs-2	Flux-4	tied to Flux-1	-0.0	0.0
Obs-9	Flux-1	0.954 ($v_{\text{line}} = 0.04c$)	-5.4	1.6
Obs-9	Flux-2	tied to Flux-1	-2.4	0.9
Obs-9	Flux-3	tied to Flux-1	-3.1	1.3
Obs-9	Flux-4	tied to Flux-1	-2.5	0.6

by some previous works (Geirliński et al. 2008; Alston et al. 2014). However, the excision of the core of PSF will cause a decrease of the S/N because of the loss of source photons, thus there is often a compromise between S/N and the pile-up level.

In Section 5.1 we applied the best-fit Model-2 of Obs-9 to the same set of variability spectra from Obs-2. To maxi-

mize the S/N for the model test, we did not excise the core of PSF for the variability spectra. Here we show the results after excising the central 10 arcsec of the PSF. Figure B1 compares the same set of variability spectra before and after the pile-up removal. Note that the time-averaged spectrum is always extracted outside the pile-up region, so the red and black time-averaged spectra are exactly the same. It is clear that the spectra are still consistent, and the spectral decompositions are not affected significantly. In this case, the main influence of the pile-up removal is the decrease of S/N. Similarly, Zoghbi & Fabian (2011) also showed that pile-up does not affect the time lag measurement for the data of Obs-2. Therefore, we can conclude that the pile-up in Obs-2 does not affect our results in this work.

This paper has been typeset from a $\text{\TeX}/\text{\LaTeX}$ file prepared by the author.

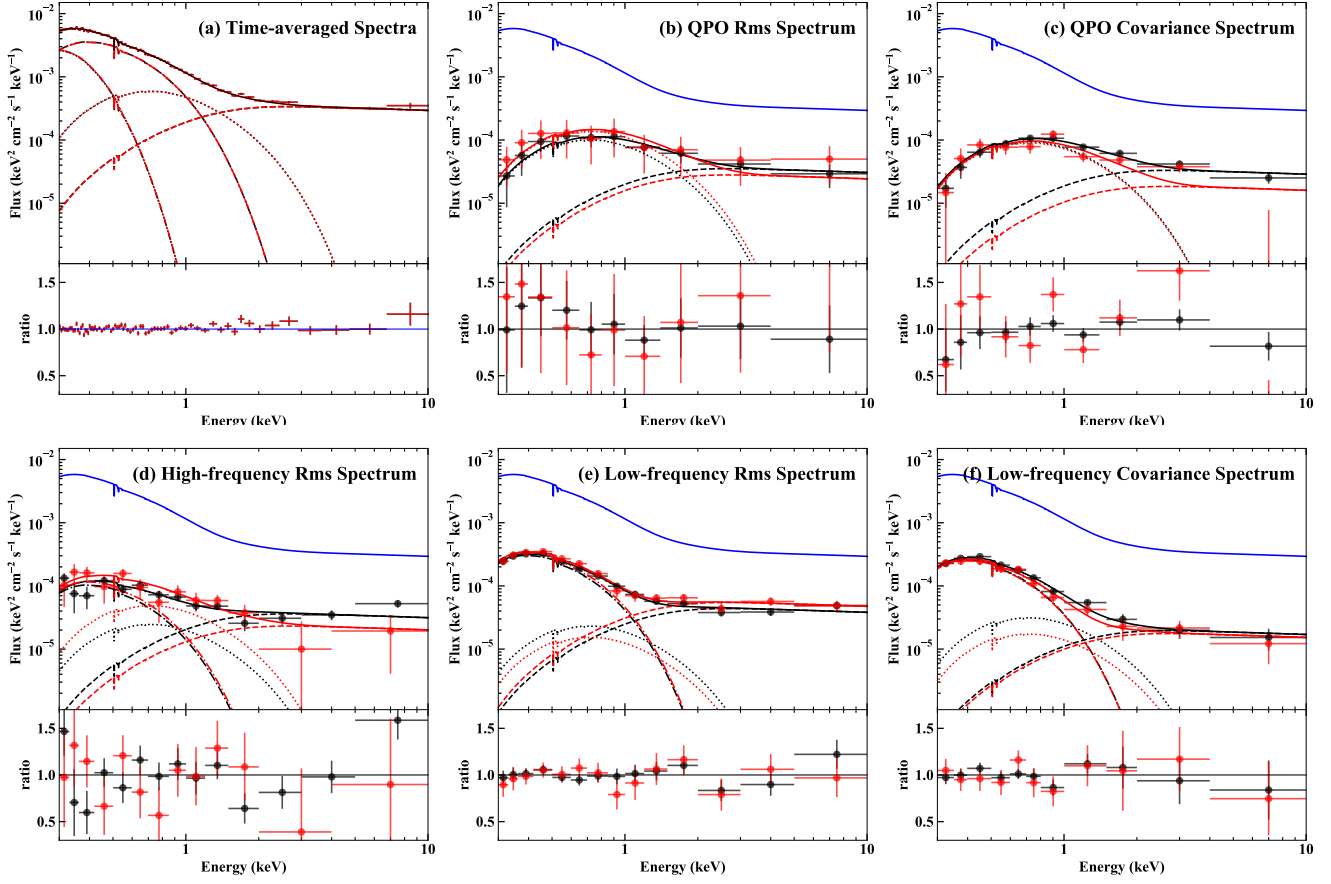


Figure B1. Comparing the variability spectra of RE J1034+396 from the data of Obs-2 using different source extraction regions. The black spectra are the same as those plotted in Figure 7. For the red spectra, the central circular region of 10 arcsec radius is excised to remove the pile-up effect. No significant differences are found between the two sets of variability spectra, except that the red spectra have lower S/N due to the loss of source photons.